Hilbert proper orthogonal decomposition: A tool for educing advective wave packets from flow field data

Marco Raiola [*]
Aerospace Engineering Department, Universidad Carlos III de Madrid, Leganés 28912, Spain and Institute of Fluid Mechanics, Karlsruhe Institute of Technology, Karlsruhe D-76131, Germany

Jochen Kriegseis
Institute of Fluid Mechanics, Karlsruhe Institute of Technology, Karlsruhe D-76131, Germany

(Received 7 November 2025; accepted 10 March 2026; published 6 April 2026)

Traveling wave packets are key coherent features contributing to the dynamics of several advective flows. This work introduces the Hilbert proper orthogonal decomposition (HPOD) to distill these features from flow field data, leveraging their mathematical representation as modulated traveling waves. The HPOD is a complex-valued extension of the proper orthogonal decomposition, where the Hilbert transform of the dataset is used to compute its analytic signal. Two versions of the technique are explored and compared: the conventional HPOD, computing the analytic signal in time, and a novel space-only HPOD, computing it along the advection direction. The HPOD is shown to extract wave packets with amplitude and frequency modulation in time and space. Its broadband nature offers an alternative to spectrally pure decompositions when instantaneous, local wave characteristics are important. The space-only version, leveraging space/time equivalence in traveling waves to swap temporal operations with spatial ones, is proven mathematically equivalent to its conventional counterpart. The two HPOD versions are characterized and validated on three datasets ordered by complexity: a two-dimensional (2D) direct numerical simulation of a laminar bluff-body wake with periodic vortex shedding; a large eddy simulation of a turbulent jet with intermittent, highly modulated wave packets; and a 2D particle image velocimetry experiment of a turbulent jet with measurement errors and no temporal resolution. In advecting flows, both HPOD versions deliver practically identical complex-valued advecting wave-packet structures, characterized by spatiotemporal amplification and decay, wave modulation, and intermittency phenomena in turbulent flow cases, such as in turbulent jets. The space-only variant allows the extraction of these structures from temporally under-resolved datasets, typical of snapshot particle image velocimetry.

DOI: 10.1103/bhlm-qwfh

I. INTRODUCTION

One of the primary challenges faced in modern fluid dynamics has become simplifying and distilling the complex dynamics of fluid flows into a more understandable form; even in

[*]Contact author: mraiola@ing.uc3m.es

seemingly simple configurations, fluid flows often exhibit intricate and unpredictable behaviors. This longstanding challenge stems from the inherent nonlinearity and chaotic nature of fluid dynamics, particularly in turbulent flows, where flow structures of various sizes and timescales dynamically interact. A key instrument to reduce the complexity of these high-dimensional flows is modal decomposition techniques, capable of dividing the problem into more manageable low-dimensional flow structures. Comprehensive reviews of these techniques can be found in the works of Rowley and Dawson [1] and Taira *et al*. [2].

In this work, we propose a data-driven modal decomposition technique specifically designed to distill spatiotemporal coherent features in advection-dominated flows. These coherent features are typically representative of the advective structures populating these flows. The vortex shedding pattern produced by the Bérnand–von Kármán instability is a clear example of advective flow structures emerging in both laminar and turbulent bluff-body wake flows [3]. Advecting structures are also observed in shear layers, where vortices are produced through the Kelvin-Helmholtz instability. This case is especially relevant in jet flows, where distinct advecting patterns, typically referred to as wave packets, have been observed to be a key component of subsonic jet noise [4]. Eduction of these flow features dates back to the early work of Arndt *et al*. [5]. In this context, modeling wave packets is a primary concern to provide a better understanding of subsonic jet noise [6], which is complicated by the presence of intermittency and modulation effects in these features. Wall-bounded flows are characterized by advecting structures at different scales: coherent waves are found in the viscous layer near the wall or as very large structures spanning the entire boundary layer, both advecting with uniform velocity; transient bursts advecting with nonuniform velocity are typically associated with the logarithmic layer [7].

Decomposition techniques are nowadays almost ubiquitous in fluid mechanics, being a preliminary step towards flow modeling, control and optimization. Data-driven decomposition techniques, in particular, have gained traction due to their flexibility and the abundance of large flow datasets generated by modern experimental and numerical methods. Among them, proper orthogonal decomposition (POD [8–10]) occupies a prominent role in terms of usage. The method is popular in other disciplines mainly with the names principal component analysis (PCA), empirical orthogonal function (EOF) analysis, and Karhunen-Loève decomposition. More specifically, the literature has been mostly dominated by a specific version of the POD, nowadays mostly referred to as *standard*, *space-only,* or *snapshot* [11–13], since it does not impose any requirement on the data fed to it—especially in terms of temporal resolution. The space-only POD identifies a set of real-valued orthonormal eigenfunctions, i.e., modes, which provide the most compact representation, in a least-squares sense, of a set of observations of the flow field, which typically represent snapshots of the field at different observation times. These modes, even if uncorrelated, may share a mutual spatiotemporal dependency due to the inability of real-valued functions to embed phase information. Advecting structures, acting as traveling wave packets, are typically split into pairs of neighboring real-valued POD modes, sharing a similar frequency content (both in time and space) but in phase quadrature. In periodic flows this dependency can be easily spotted by reconstructing the temporal modes in so-called Lissajous figures, which reveal the phase relation in the corresponding shape of the resulting cyclograms (see, e.g., [14,15]). Simple oscillator models can be constructed by summing these pairs as real and imaginary parts of a complex-valued mode [16]. Since spatiotemporal coherence is not enforced in the original POD problem, however, modes in more complex flow scenarios (e.g., involving broadband phenomena and/or nonstationary behaviors) may fail to provide a clear set of conjugate mode pairs, making it difficult to use POD for describing traveling features.

An alternative decomposition, the dynamic mode decomposition (DMD), was developed by Schmid [17] to specifically identify coherent flow structures describing the flow dynamics, i.e., the evolution of the flow through time. The work was motivated by the loss of dynamical information produced by the space-only POD, specifically due to the averaging process used to obtain the spatial correlation tensor. DMD is based on the eigendecomposition of a best-fit linear operator that approximates the dynamics present in the data. Its eigenvalues can be interpreted as the

temporal evolution embedded in the linear dynamics tensor, i.e., complex-valued frequencies of an exponential function, making DMD a data-driven equivalent to linear stability analysis. The capability of DMD to decompose the dynamics of the flow, roots itself in the Koopman theory [18], consisting of approximating nonlinear dynamical systems with a much larger (typically infinite dimensional) linear ones. A deeper review of the connection between Koopman analysis and DMD can be found in [19–21].

For statistically stationary flows, spatiotemporal coherent modes can be extracted by the spectral proper orthogonal decomposition (SPOD [9,22]), which restates the original POD problem in the frequency space rather than in temporal coordinates. Unlike space-only POD, which is based on the decomposition of the two-point correlation matrix, the SPOD extracts the modes from the cross-spectral density matrix for each specific temporal frequency. This results in a set of orthogonal complex-valued spatial modes each linked to a harmonic temporal evolution. As such, SPOD provides a decomposition which is spatiotemporally coherent. In particular, thanks to the translation properties of the Fourier transform, SPOD has become one of the standard techniques to extract advecting patterns, as, for example, with wave packets in turbulent jets [6]. One of the main drawbacks of the technique, however, stems from the hypothesis of statistical stationarity and the use of the Fourier transform: the temporal evolution is fixed to follow a pure harmonic relation having infinite temporal support, i.e., extending up to infinity, thus losing any instantaneous character of the temporal evolution. Additionally, SPOD imposes spectral purity on the temporal coefficients of the modes, thus separating into different modes coherent structures with multiple frequency content. This is especially problematic in highly turbulent flows, where coherent structures can be characterized by strong intermittency and variable frequency due to phase jitter or frequency modulations. In these cases, a single physical feature is, therefore, likely to be split among multiple SPOD modes. Finally, it is worth highlighting that, by splitting the original POD problem into frequency-fixed bins, the SPOD would maintain the orthogonality constraint only between modes extracted from the same bin. This is especially challenging if a compact representation of the flow is sought.

Alternative extensions of the POD have been proposed by Sieber *et al*. [23] and Mendez *et al*. [24] blending discrete Fourier transform (DFT) and POD. Sieber's spectral proper orthogonal decomposition (not to be confused with the one proposed in the original work by Lumley [9] and repopularized by Towne *et al*. [22]) applies a low-pass filter along the diagonals of the temporal correlation matrix before computing the POD according to the snapshot method. This filter forces the matrix to assume a form closer to a Toeplitz circulant matrix, whose eigenfunctions are Fourier modes, according to the Szegö theorem [25]. Depending on the filter size, the method can blend between pure DFT and pure POD. The multiscale proper orthogonal decomposition (mPOD) introduced by Mendez *et al*. [24] combines the idea of windowed SPOD (borrowed from Sieber *et al*. [23]) and the SPOD by Towne *et al*. [22]. Instead of filtering the correlation matrix as in [23], the mPOD decomposes it into the contributions of different scales using the multiresolution architecture. Instead of computing various eigenbases from the spectra of different portions of the data, as in Towne *et al*. [22], the mPOD computes eigenbases on the correlation matrix of different scales. While these techniques can provide a decomposition with a more complex spectral behavior and preserving the orthogonality constraint between modes with different frequency content, they also introduce user-dependent parameters in the process, thus effectively not delivering a univocal decomposition.

Kriegseis *et al*. [26] introduced in the field of fluid mechanics an extension of the POD, under the name of Hilbert proper orthogonal decomposition (HPOD), which can automatically deliver complex-valued modes satisfying the conditions to build oscillator models. The method is rooted in the analytic signal concept to obtain a complex-valued extension of flow-field time series prior to performing the space-only POD. The complex-valued extension is obtained through the Hilbert transform [27], adding to the original time series an imaginary part shifted by $\pi/2$ in time, independently of the frequency content, to build the analytic signal of the field time series. The HPOD on time series, however, requires time-resolved field data, converging to standard POD

when undersampled data are used [26]. The use of the Hilbert transform and analytic signal in the temporal direction for fluid mechanics applications is indeed not novel: examples of it can be found for measuring the intermittency in turbulence phenomena [28], for identifying envelope modulation of fine turbulence scales [29], or for tracking the spatiotemporal evolution of perturbations in under-expanded supersonic jet [30]. Additionally, the Hilbert-Huang transform, involving the successive application of empirical mode decomposition and the temporal Hilbert transform, has been applied for the time-frequency analysis of turbulent data in both the Eulerian [31–33] and Lagrangian [34] frames.

While the name HPOD has been used for the first application to flow field analysis, the technique was originally introduced with different names in several fields of study. The first application of the technique, under the name of complex empirical orthogonal functions (COEF), targeted the identification of coherent propagating features in gridded wind data for meteorological applications, where the short-term irregular nature of some of the features made common spectral analysis inappropriate [35–37]. Horel [38] demonstrated the soundness of the technique, renamed complex principal components (CPC) analysis, to extract traveling and standing waves from geophysical data. Pfeffer *et al*. [39] applied CPC analysis in a thermally driven, rotating annulus fluid flow with sinusoidal bottom topography for meteorological applications. The limitation of the COEF in isolating wideband propagating waves has been studied by Merrifield and Guza [40]. CPC analysis has been used to analyze the temporal variation of sea surface temperature [41]. Feeny [42] introduced the technique under the name complex orthogonal decomposition (COD) for identifying wave motion in vibration analysis, also proposing an index to classify standing and traveling waves. COD has been used for the kinematic study of flexible structures in fluid-structure interaction applications [43,44]. CPC analysis has been applied to the temporal variation of the Antarctic ice sheet [45] as well as to MRI data to study the organization of the human brain [46].

Other strategies to identify traveling features involve a change of the reference frame in which space-only POD is performed. As pointed out by Brunton and Kutz [47], traveling features introduce translation symmetries in the fields, which disrupt the spatial alignment of coherent features between snapshots and therefore corrupt the correlation matrix, providing a decomposition which splits features over multiple modes. To provide a correct application of the space-only POD, translation invariance must be taken into account. For wavelike patterns, this involves accounting for the phase velocity of the wave. Procedures like *centering* [48], i.e., shifting the wave so that centers align between frames, or *template fitting* [49,50], i.e., shifting the data so as to maximize the correlation with a preselected template, allow accounting for a single advecting velocity. Multiple advecting velocities can be accounted for through the *shifted* POD [51], where modes advecting at different velocities are separated into different reference frames through an iterative procedure. This class of strategies to identify advecting features relies on the estimation of the advection velocity and on using it to correct the translation symmetry explicitly.

Following a similar logic of correcting for the translation symmetry through a reference frame transformation, Sesterhenn and Shahirpour [52] introduced the concept of performing the decomposition in a spatiotemporal direction characteristic of the traveling structure. This transformation is introduced by performing a rotation in the spatial and temporal dimensions of the data, identifying the rotation—and hence the advection velocity—maximizing the difference between the first two singular values. Performing the modal analysis in a direction different from the temporal one has already been exploited several times for advecting features. Schmid [17] also considers performing the DMD in the spatial direction rather than the temporal one to provide a data-driven *spatial stability analysis*. This same idea was later exploited by Ek *et al*. [53] to produce the *permuted* POD. By reorienting the data matrix along the advection direction through permutation prior to performing standard POD, they produced modes, which are orthogonal in time and in the remaining spatial directions. Similar approaches can also be identified in non-data-driven decompositions. For example, Encinar and Jiménez [54] applied complex wavelet analysis in the advection direction to identify wavetrains in turbulent channel flows.

All the decompositions targeting traveling features reported so far rely on the availability of temporally resolved data in order to enforce the spatiotemporal coherence of the modes. When no temporal resolution is available, only standard POD can be applied, trying to reconstruct spatiotemporal coherent features by pairing real-valued modes. The present work elaborates on the capabilities of HPOD to provide a decomposition targeting traveling wave flow features and introduces a *space-only* version of the technique, which does not require temporal resolution of the data. This *space-only* HPOD is based on computing the analytic signal from the Hilbert transform in the advection direction, instead of in the temporal direction of the dataset, as in the *conventional* HPOD. This means that the imaginary part of the analytic signal is shifted by $\pi/2$ along the advection direction with respect to the original real-valued signal. Therefore, the space-only HPOD can target advecting wave packets by leveraging the similarity between time and the advection direction in advecting flows. In this sense, the approach has some connection with the permuted POD by Ek *et al*. [53].

Section II presents a general framework for both the conventional and space-only HPOD, introducing the properties of the decomposition, providing the interpretation of the complex-valued wave packet functions as analytic signals, and demonstrating that both conventional and space-only HPOD deliver eigenfunctions, which are analytic signals in time for advecting flows. Section III provides three different test cases to demonstrate the properties of the HPOD and highlight its capabilities. The first dataset is a direct numerical simulation (DNS) of a laminar wake of a cylinder, with a compact and spectrally pure shedding signature, used to demonstrate the properties of both the conventional and space-only HPOD. The second test case is the large eddy simulation (LES) of a turbulent jet, featuring more complex wave packets, which is used to show the capabilities of HPOD to capture amplitude-modulated and wideband traveling waves. The third dataset, including the velocity fields of a turbulent jet measured via snapshot particle image velocimetry (PIV), is used to showcase the robustness of the space-only HPOD in real experimental scenarios. Finally, Sec. IV draws the conclusions on both HPODs versions, suggesting their possible role in the toolbox of researchers in the field of fluid mechanics.

II. MATHEMATICAL BACKGROUND

A. Standard proper orthogonal decomposition

The *standard* (also referred to as *space-only*) proper orthogonal decomposition (POD) aims to determine the set of functions $\psi_j(t)$ and $\boldsymbol{\phi}_j(\boldsymbol{x})$, which best approximates a field $\boldsymbol{u}(\boldsymbol{x},t)$. Here $\boldsymbol{x}=(x,y,z)$ and t represent the spatial and temporal coordinates, respectively. In the following, the biorthogonal formulation introduced by [13] will be followed and recapped to describe the mathematical framework of this method. The decomposition of $\boldsymbol{u}$ aims to identify a set of temporal orthogonal modes ψ_j and spatial orthogonal modes $\boldsymbol{\phi}_j$ so that

$$\boldsymbol{u}(\boldsymbol{x},t)=\sum_j \psi_j(t)\sigma_j\boldsymbol{\phi}_j(\boldsymbol{x}), \tag{1}$$

where σ_j is the singular value associated to each ψ_j and $\boldsymbol{\phi}_j$. Notice that σ_j is always a non-negative real. The functions ψ_j and $\boldsymbol{\phi}_j$, instead, will be either real- or complex-valued—depending on whether the original field $\boldsymbol{u}$ is real- or complex-valued. Both the functions $\boldsymbol{\phi}_j$ and ψ_j form an orthogonal basis, i.e.,

$$\int_\Omega \boldsymbol{\phi}_j(\boldsymbol{x})\boldsymbol{\phi}_k^*(\boldsymbol{x})\mathrm{d}\boldsymbol{x}=\delta_{jk},\quad \int_T \psi_j(t)\psi_k^*(t)\mathrm{d}t=\delta_{jk}, \tag{2}$$

where Ω and T refer to the spatial and temporal domain over which the field is considered.

The decomposition in Eq. (1) is solved by identifying the set of orthogonal functions $\boldsymbol{\phi}_j$ solving the two equivalent minimization or maximization problems

$$\min_{\boldsymbol{\phi}} \left\langle \left\| \boldsymbol{u} - \frac{\int_\Omega \boldsymbol{u}(\boldsymbol{x},t)^* \boldsymbol{\phi}_j(\boldsymbol{x}) \mathrm{d}\boldsymbol{x}}{\|\boldsymbol{\phi}_j(\boldsymbol{x})\|_x^2} \boldsymbol{\phi}_j(\boldsymbol{x}) \right\|_x^2 \right\rangle \Leftrightarrow \max_{\boldsymbol{\phi}} \frac{\left\langle \left| \int_\Omega \boldsymbol{u}(\boldsymbol{x},t)^* \boldsymbol{\phi}_j(\boldsymbol{x}) \mathrm{d}\boldsymbol{x} \right|^2 \right\rangle}{\|\boldsymbol{\phi}_j(\boldsymbol{x})\|_x^2}, \tag{3}$$

where * indicates the complex conjugate, $\langle \cdot \rangle$ indicates the ensemble average and $\| \cdot \|_x^2$ indicates the spatial norm $\|f\|_x^2 = \int_\Omega f^*(\boldsymbol{x}) f(\boldsymbol{x}) \mathrm{d}\boldsymbol{x}$. Similarly, the decomposition can be restated as the identification of the set of functions ψ_j solving the minimization or maximization problems

$$\min_{\psi} \left\langle \left\| \boldsymbol{u} - \frac{\int_T \boldsymbol{u}(\boldsymbol{x},t)^* \psi_j(t) \mathrm{d}t}{\|\psi_j(t)\|_t^2} \psi_j(t) \right\|_t^2 \right\rangle \Leftrightarrow \max_{\psi} \frac{\left\langle \left| \int_T \boldsymbol{u}(\boldsymbol{x},t)^* \psi_j(t) \mathrm{d}t \right|^2 \right\rangle}{\|\psi_j(t)\|_t^2}, \tag{4}$$

where $\| \cdot \|_t^2$ indicates the temporal norm $\|f\|_t^2 = \int_T f^*(t) f(t) \mathrm{d}t$.

The ensemble average $\langle \cdot \rangle$ in Eqs. (3) and (4) is typically defined either as the average of the samples in time (for the spatial norm problem) or space (for the time norm problem) when considering standard POD. The solution of the problem in Eq. (3) is given by the Fredholm integral equation

$$\int_\Omega C(\boldsymbol{x}, \boldsymbol{x}', t = t') \boldsymbol{\phi}_j(\boldsymbol{x}') \mathrm{d}\boldsymbol{x}' = \sigma_j^2 \boldsymbol{\phi}_j(\boldsymbol{x}), \tag{5}$$

which represents the eigenvalue problem for the two-(space)-point correlation function $C(\boldsymbol{x}, \boldsymbol{x}', t = t')$

$$C(\boldsymbol{x}, \boldsymbol{x}', t = t') = \langle \boldsymbol{u}(\boldsymbol{x},t) \boldsymbol{u}^*(\boldsymbol{x}', t') \rangle = \int_T \boldsymbol{u}(\boldsymbol{x},t) \boldsymbol{u}^*(\boldsymbol{x}', t) \mathrm{d}t. \tag{6}$$

Similarly, the solution for the problem in Eq. (4) is provided by the eigenvalue problem

$$\int_T C(\boldsymbol{x} = \boldsymbol{x}', t, t') \psi_j(t') \mathrm{d}t' = \sigma_j^2 \psi_j(t), \tag{7}$$

where $C(\boldsymbol{x} = \boldsymbol{x}', t, t')$ is the two-(time)-instant correlation function

$$C(\boldsymbol{x} = \boldsymbol{x}', t, t') = \langle \boldsymbol{u}(\boldsymbol{x},t) \boldsymbol{u}^*(\boldsymbol{x}', t') \rangle = \int_\Omega \boldsymbol{u}(\boldsymbol{x},t) \boldsymbol{u}^*(\boldsymbol{x}, t') \mathrm{d}\boldsymbol{x}. \tag{8}$$

Following the biorthogonal approach, the orthogonal temporal and spatial modes are obtained as the eigenfunctions of the two symmetric eigenvalue problems in space [Eq. (5)] and time [Eq. (7)]. These modes are not independent one from the other, sharing instead a one-to-one correspondence between spatial and temporal parts, as shown by Eq. (1). In the following, the denomination proposed by Aubry [12] will be adopted, referring to each term of the summation in Eq. (1)—i.e., a pair of temporal and spatial modes (ψ_j and $\boldsymbol{\phi}_j$) and their associated eigenvalue (σ_j)—as *structure*.

The adjective *space-only*, oftentimes used to refer to this decomposition, reflects the fact that spatiotemporal coherency is not considered, i.e., the problem either solves the eigenvalue problem for zero-time-lag spatial correlation matrix or the zero-space-shift temporal correlation matrix. In this sense, the decomposition is not guaranteed to effectively track coherent flow features, which evolve through time and space. Also, the nomenclature used here suggests that the two-point and the two-instant correlation matrices are special cases of the space-time correlation tensor

$$C(\boldsymbol{x}, \boldsymbol{x}', t, t') = \langle \boldsymbol{u}(\boldsymbol{x},t) \boldsymbol{u}^*(\boldsymbol{x}', t') \rangle, \tag{9}$$

whose eigenvalue problem produces the *space-time* POD.

B. Wave-packet interpretation of coherent structures

The aim of this work is to identify coherent features evolving spatiotemporally in advective flows. These features can be interpreted as wave packets traveling in the flow direction. A single wave packet can be represented (here in one dimension for ease of notation) as a sinusoidal function,

$$w_j(x,t) = A_j(x,t)\cos(k_j x - \omega_j t) = A_j(x,t)\cos[k_j(x - c_j t)], \tag{10}$$

where A_j represents its instantaneous and local amplitude, k_j its spatial angular wave number, ω_j its temporal angular frequency and $c_j = \omega_j/k_j$ its wave velocity. This wave packet can be considered as the real part of a complex-valued wave, constructed by adding a companion imaginary sinusoidal function shifted $\pi/2$ with respect to the original wave,

$$w_j(x,t) = A_j(x,t)\mathrm{Re}[\cos(k_j x - \omega_j t) + i\sin(k_j x - \omega_j t)] = A_j(x,t)\mathrm{Re}\left[e^{i(k_j x - \omega_j t)}\right], \tag{11}$$

where Re indicates that the real part of the function should be taken, i indicating the imaginary unit and where the equality with the exponential function follows from Euler's formula. It is worth noticing that the sinusoidal functions can be further decomposed using the trigonometric formulas

$$e^{i(k_j x - \omega_j t)} = [\cos(k_j x)\cos(\omega_j t) + \sin(k_j x)\sin(\omega_j t)] + i[\sin(k_j x)\cos(\omega_j t) - \cos(k_j x)\sin(\omega_j t)]. \tag{12}$$

The imaginary part of Eq. (12) can be interpreted both as a $\pi/2$ phase shift operated on the temporal sinusoidal functions, i.e.,

$$\begin{aligned} e^{i(k_j x - \omega_j t)} &= \cos(k_j x)[\cos(\omega_j t) - i\sin(\omega_j t)] + \sin(k_j x)[\sin(\omega_j t) + i\cos(\omega_j t)] \\ &= F(x,t) + iF\left(x, t + \frac{1}{\omega_j}\frac{\pi}{2}\right), \end{aligned} \tag{13}$$

or as a phase shift on the spatial ones, i.e.,

$$\begin{aligned} e^{i(k_j x - \omega_j t)} &= \cos(\omega_j t)[\cos(k_j x) + i\ \sin(k_j x)] + \sin(\omega_j t)[\sin(k_j x) - i\ \cos(k_j x)] \\ &= F(x,t) + iF\left(x + \frac{1}{k_j}\frac{\pi}{2}, t\right). \end{aligned} \tag{14}$$

Note that the description of the real-valued part of the wave requires the sum of two separate sinusoidal functions, both in space and time. When space-only POD is applied to these data, it will try to retrieve these two functions as two separate orthogonal modes, without any guarantee not to distort any of them with spurious not-matching frequency content. On the contrary, in the complex domain, the wave can be more compactly represented by one complex exponential in space and time, reducing the number of modes needed and avoiding the possibility of distortions. Therefore, to extract the wave packets from a given flow field, including all their phase and amplitude information, the data need to be extended to the complex domain. This operation is termed *complexification* and is described in the following section.

C. Complexification of the flow field

Several techniques can be applied to obtain a complex-valued version of the flow field. Spectral POD [22,55], for example, performs a Fourier decomposition in time over the flow field sequence. According to this complexification, the SPOD is the result of an eigenvalue problem on the cross-spectral density tensor. However, this means that the sequence, and therefore the resulting modes, is expressed in the frequency space.

An alternative operation, popular in signal analysis, is the computation of the analytic signal, which consists in removing the redundant negative frequency components from the original real signal. This operation recovers a complex-valued signal whose real part is identical to the original signal, and which has a single-sided spectrum that preserves the original signal frequency content.

The analytic signal is typically constructed by adding to the original real-valued signal an imaginary signal obtained from the Hilbert transform of the original signal. For one-dimensional real-valued temporal signal $s(t)$, the analytic signal is then expressed as

$$\tilde{s}(t) = s(t) + i\,\mathcal{H}_t[s(t)], \tag{15}$$

where i is the imaginary unit and $\mathcal{H}_t$ is the Hilbert transform operator [27] applied in time and defined as the Cauchy principal value of the convolution of $s(t)$ with the signal $1/\pi t$ according to

$$\mathcal{H}_t[s(t)] = \lim_{e\to 0} \int_{|\tau - t|>e} \frac{s(\tau)}{\pi(t-\tau)} \mathrm{d}\tau = \frac{1}{\pi t} * s(t), \tag{16}$$

where $*$ indicates the convolution operation. The analytic signal of $s(t)$ can therefore be written using the convolution notation as

$$\tilde{s}(t) = \left(\delta(t) + \frac{i}{\pi t}\right) * s(t), \tag{17}$$

with $\delta(t)$ being the Dirac delta function.

The Hilbert transform can be interpreted in the Fourier space as a $\pi/2$ shift, either in advance or delay depending on the sign of the frequency component. If $\mathcal{F}$ is used to indicate the Fourier transform [27]:

$$\mathcal{F}\{\mathcal{H}[s]\}(f) = -\mathrm{sgn}(f) e^{-i\frac{\pi}{2}} \mathcal{F}[s](f) = -i\,\mathrm{sgn}(f)\mathcal{F}[s](f), \tag{18}$$

which leads to the following expression for the analytic signal:

$$\tilde{s}(t) = \mathcal{F}^{-1}\{[1 + i\,\mathrm{sgn}(f)]\mathcal{F}[s(t)]\}. \tag{19}$$

This expression shows that the analytic signal shares the same frequency content of the original signal for positive frequencies, while the content for negative frequencies is discarded. Additionally, this expression provides the operative definition used in this work for the computation of the analytic signal from a discrete signal: the fast Fourier transform (FFT) of the signal is first computed, then negative frequency terms are set to zero while positive frequency terms are doubled, and finally the inverse FFT is applied (see [56]). It is worth highlighting at this point that, since FFT is involved, this algorithm does not recover the exact analytic signal for finite sequences due to the edge effects introduced by the Fourier transform (see [57]). These edge effects are typically treated by removing the corrupted part of the signal before further analyses are carried out. The implications of these errors on the proposed technique will be exemplified in Sec. III A. Other techniques to correct edge effects might involve padding or windowing of the original signal or the use of algorithm not involving FFT [57], which, however, will not be explored in this work.

The analytic signal obtained for an oscillatory signal can be interpreted as a generalized phasor of the original signal, according to the polar representation for complex values

$$\tilde{s}(t) = |s(t)| e^{\varphi(t)}, \tag{20}$$

which contains information on its instantaneous amplitude $|s(t)|$ and phase $\varphi(t)$. This concept is at the basis of the Hilbert spectral analysis, which allows to extract the instantaneous frequency of a signal as

$$f(t) = \frac{1}{2\pi}\frac{\mathrm{d}\varphi(t)}{\mathrm{d}t}. \tag{21}$$

The Hilbert transform in time can be extended to a generic real-valued velocity field $\boldsymbol{u}(x, y, z, t)$ to obtain its complex-valued analytic representation

$$\tilde{\boldsymbol{u}}(x, y, z, t) = \boldsymbol{u}(x, y, z, t) + i\,\mathcal{H}_t[\boldsymbol{u}(x, y, z, t)] \tag{22}$$

with

$$\mathcal{H}_t[\boldsymbol{u}(x,y,z,t)] = \lim_{e\to 0}\frac{1}{\pi}\int_{|\tau-t|>e}\frac{\boldsymbol{u}(x,y,z,\tau)}{t-\tau}\mathrm{d}\tau. \tag{23}$$

Alternatively, the Hilbert transform $\mathcal{H}$ can be defined along one of the spatial directions. Assuming an advection-dominated flow, with x being the direction in which the flow structures are advected, this operation would provide an analytic representation whose imaginary part is shifted by $\pi/2$ in the x direction. This would result in the analytic representation

$$\tilde{\boldsymbol{u}}(x,y,z,t) = \boldsymbol{u}(x,y,z,t) + i\,\mathcal{H}_x[\boldsymbol{u}(x,y,z,t)] \tag{24}$$

with $\mathcal{H}_x$ being the Hilbert transform in the advection direction, i.e.,

$$\mathcal{H}_x[\boldsymbol{u}(x,y,z,t)] = \lim_{e\to 0}\frac{1}{\pi}\int_{|\xi-x|>e}\frac{\boldsymbol{u}(\xi,y,z,t)}{x-\xi}\mathrm{d}\xi. \tag{25}$$

While the two analytic representations of a flow field might appear contrasting, they can be reconciled if the flow field is assumed to behave as a wave packet. In fact, following Sec. II B, it can be shown that

$$\begin{aligned} e^{i(k_j x-\omega_j t)} &= f(x,t) + i\,f\left(x, t+\frac{1}{\omega_j}\frac{\pi}{2}\right) = f(x,t) + i\,\mathcal{H}_t[f(x,t)] \\ &= f(x,t) + i\,f\left(x+\frac{1}{k_j}\frac{\pi}{2}, t\right) = f(x,t) + i\,\mathcal{H}_x[f(x,t)]. \end{aligned} \tag{26}$$

Since the Hilbert transform is a linear operator, the same can be applied to a field composed of a sum of wave packets. Based on this concept, the proposed complexification of the flow field allows for recognizing complex-valued wave packets. In the following, a complex-valued version of the POD is introduced, which allows the distilling of wave-packet-like features from the complexified flow field.

D. Hilbert proper orthogonal decomposition in time and space

Once the field has been extended to complex values, applying the standard POD as introduced in Sec. II A is possible. The decomposition of $\tilde{\boldsymbol{u}}$ identifies a set of complex-valued temporal (ψ_j) and spatial ($\boldsymbol{\phi}_j$) orthogonal modes, i.e.,

$$\tilde{\boldsymbol{u}}(\boldsymbol{x},t) = \sum_j \psi_j(t)\sigma_j\boldsymbol{\phi}_j(\boldsymbol{x}), \tag{27}$$

resulting from the solution of the eigenvalue problem for the two-(space)-point correlation function of the analytic field representations

$$\int_\Omega \tilde{C}(\boldsymbol{x},\boldsymbol{x}',t=t')\boldsymbol{\phi}_j^*(\boldsymbol{x}')\mathrm{d}\boldsymbol{x}' = \sigma_j^2\boldsymbol{\phi}_j(\boldsymbol{x}),\quad \tilde{C}(\boldsymbol{x},\boldsymbol{x}',t=t') = \int_T \tilde{\boldsymbol{u}}(\boldsymbol{x},t)\tilde{\boldsymbol{u}}^*(\boldsymbol{x}',t)\mathrm{d}t, \tag{28}$$

or, similarly, of the eigenvalue problem for the two-(time)-instant correlation function

$$\int_T \tilde{C}(\boldsymbol{x}=\boldsymbol{x}',t,t')\psi_j^*(t')\mathrm{d}t' = \sigma_j^2\psi_j(t),\quad \tilde{C}(\boldsymbol{x}=\boldsymbol{x}',t,t') = \int_\Omega \tilde{\boldsymbol{u}}(\boldsymbol{x},t)\tilde{\boldsymbol{u}}^*(\boldsymbol{x},t')\mathrm{d}\boldsymbol{x}. \tag{29}$$

Since the correlation matrix is obtained from analytic signals, the eigenfunctions obtained from this approach would be analytic signals as well, i.e., they would have zero negative-frequency content. A proof of this is provided in the following section. Therefore, the HPOD eigenfunctions would allow the extraction of instantaneous/local frequency, phase and amplitude of each eigenfunction, similarly to what would be possible through an Hilbert spectral analysis.

E. The analytic signal nature of HPOD eigenfunctions

It is possible to prove that the HPOD problem delivers eigenfunctions, which are analytic signals, i.e., that their spectral content is limited to positive frequency only. Consider the analytic signal of the temporal correlation function $\tilde{C}$. Its relation with the cross-spectral density function is given by

$$\tilde{C}(x,x',t,t') = \tilde{C}(x,x',t,\tau) = \int_{-\infty}^{\infty} [1+\mathrm{sgn}(\omega)] S(x,x',t,\omega) e^{i\omega\tau} \mathrm{d}\omega, \tag{30}$$

where $S(x,x',t,\omega)$ is the cross-spectral density function at an instant t (in the time-frequency sense), ω represent the temporal angular frequency, and $\tau = t - t'$ (see, e.g., [27]). Notice that for ease of notation a single spatial coordinate, i.e., the advection direction, is considered in the following, but results will be equally valid for multiple spatial coordinates. In Eq. (30) the Fourier transform and the Hilbert transform are taken in the temporal direction. The temporal POD problem over an infinite temporal interval is given by

$$\int_{-\infty}^{\infty} \tilde{C}(x,x',t,\tau) \boldsymbol{w}(x',t') \mathrm{d}t' = \sigma^2 \boldsymbol{w}(x,t). \tag{31}$$

Substituting the Fourier transform of $\tilde{C}$ yields

$$\begin{aligned}
\int_{-\infty}^{\infty} \left[\int_{-\infty}^{\infty} [1+\mathrm{sgn}(\omega)] S(x,x',t,\omega) e^{i\omega\tau} \mathrm{d}\omega \right] \boldsymbol{w}(x',t') \mathrm{d}t' &= \sigma^2 \boldsymbol{w}(x,t), \\
\int_{-\infty}^{\infty} [1+\mathrm{sgn}(\omega)] S(x,x',t,\omega) e^{i\omega t} \left[\int_{-\infty}^{\infty} \boldsymbol{w}(x',t') e^{-i\omega t'} \mathrm{d}t' \right] \mathrm{d}\omega &= \sigma^2 \boldsymbol{w}(x,t), \\
\int_{-\infty}^{\infty} [1+\mathrm{sgn}(\omega)] S(x,x',t,\omega) e^{i\omega t} \mathcal{F}[\boldsymbol{w}](x',\omega) \mathrm{d}\omega &= \sigma^2 \boldsymbol{w}(x,t).
\end{aligned} \tag{32}$$

Assuming spectrally pure eigenfunctions (or equivalently a single component of the Fourier expansion of said eigenfunctions), the eigenfunction and its Fourier transform are

$$\boldsymbol{w}(x,t) = \boldsymbol{q}(x,\omega') e^{i\omega' t}, \quad \mathcal{F}[\boldsymbol{w}](x,\omega) = \boldsymbol{q}(x,\omega')\delta(\omega-\omega'). \tag{33}$$

Substituting (33) into the eigenproblem of (32) then leads to

$$\int_{-\infty}^{\infty} [1+\mathrm{sgn}(\omega)] S(x,x',t,\omega) e^{i\omega t} \boldsymbol{q}(x',\omega') \delta(\omega-\omega') \mathrm{d}\omega = \sigma^2 \boldsymbol{q}(x,\omega') e^{i\omega' t}. \tag{34}$$

Now it is possible to divide the eigenproblem (34) in two, depending on the sign of ω,

$$\begin{aligned}
&\text{if } \omega < 0: \quad 0 = \sigma^2 \boldsymbol{q}(x,\omega) \\
&\text{if } \omega > 0: \quad S(x,x',t,\omega)\boldsymbol{q}(x',\omega) = \tfrac{\sigma^2}{2} \boldsymbol{q}(x,\omega).
\end{aligned} \tag{35}$$

The previous equation shows that the eigenproblem solved for the HPOD in time produces temporal eigenfunctions with only positive frequencies, i.e., eigenfunctions, which are analytic signals.

Considering instead the analytic signal of the spatial correlation function

$$\tilde{C}(x,x',t,t') = \tilde{C}(x,\xi,t,t') = \int_{-\infty}^{\infty} [1+\mathrm{sgn}(k)] S(x,k,t,t') e^{ik\xi} \mathrm{d}k, \tag{36}$$

where $S(x,k,t,t')$ is the cross-spectral density function at a given position x, k represent the spatial angular wave number, and $\xi = x - x'$. In Eq. (36) the Fourier transform and the Hilbert transform are taken in the spatial direction. The spatial POD problem over an infinite spatial interval is given

by

$$\int_{-\infty}^{\infty} \tilde{C}(x,\xi,t,t')\boldsymbol{w}(x',t')\mathrm{d}x' = \sigma^2 \boldsymbol{w}(x,t). \tag{37}$$

As above, substituting the Fourier transform of $\tilde{C}$ yields

$$\int_{-\infty}^{\infty}\left[\int_{-\infty}^{\infty}[1+\mathrm{sgn}(k)]S(x,k,t,t')e^{ik\xi}\mathrm{d}k\right]\boldsymbol{w}(x',t')\mathrm{d}x' = \sigma^2\boldsymbol{w}(x,t),$$

$$\int_{-\infty}^{\infty}[1+\mathrm{sgn}(k)]S(x,k,t,t')e^{ikx}\left[\int_{-\infty}^{\infty}\boldsymbol{w}(x',t')e^{-ikx'}\mathrm{d}x'\right]\mathrm{d}k = \sigma^2\boldsymbol{w}(x,t),$$

$$\int_{-\infty}^{\infty}[1+\mathrm{sgn}(k)]S(x,k,t,t')e^{ikx}\mathcal{F}[\boldsymbol{w}](k,t')\mathrm{d}k = \sigma^2\boldsymbol{w}(x,t). \tag{38}$$

The eigenfunction and its Fourier transform can be assumed to be

$$\boldsymbol{w}(x,t) = \boldsymbol{q}(k',t)e^{ik'x}, \quad \mathcal{F}[\boldsymbol{w}](k,t) = \boldsymbol{q}(k',t)\delta(k-k'), \tag{39}$$

which substituted into the eigenproblem of Eq. (38) leads to

$$\int_{-\infty}^{\infty}[1+\mathrm{sgn}(k)]S(x,k,t,t')e^{ikx}\boldsymbol{q}(k',t')\delta(k-k')\mathrm{d}k = \sigma^2\boldsymbol{q}(k',t)e^{ik'x}. \tag{40}$$

Again, it is possible to divide the eigenproblem in two, depending on the sign of k according to

$$\begin{aligned} &\text{if } k<0: \quad 0 = \sigma^2\boldsymbol{q}(k,t) \\ &\text{if } k>0: \quad S(x,k,t,t')\boldsymbol{q}(k,t') = \tfrac{\sigma^2}{2}\boldsymbol{q}(k,t), \end{aligned} \tag{41}$$

which proves that the eigenproblem solved for the HPOD in space produces spatial eigenfunctions that are analytic signals.

F. Spatiotemporal nature of the HPOD for advecting wave packets and its relation with SPOD

In the previous section, it has been demonstrated that the conventional HPOD delivers temporal modes, which are analytic signals; conversely, space-only HPOD has demonstrated to provide spatial modes, which are analytic signals. It is possible to show that for structures capturing advecting features both temporal and spatial modes need to be analytic under the assumption that the spatiotemporal evolution is dictated by a phase velocity relationship. This translates in the two HPOD approaches being equivalent for a traveling wave packet. In the following, this property is demonstrated in the setting of stationary and homogeneous fields, both for ease of development as well to highlight the linking points with another popular decomposition technique, the SPOD.

For a stationary and homogeneous (in the advection direction x) field, the analytic signal of the time-space correlation tensor $C(x,x',t,t')$ is given by

$$\tilde{C}(x,x',t,t') = \tilde{C}(\xi,\tau) = \int_{-\infty}^{\infty}[1+\mathrm{sgn}(k)]S(k,\omega)e^{i(k\xi-\omega\tau)}\mathrm{d}k, \tag{42}$$

where $S(k,\omega)$ is the cross-spectral density tensor, k and ω, respectively, represent the angular wave number and frequency in space and time, and

$$\xi = x - x', \quad \tau = t - t'. \tag{43}$$

In Eq. (42) the Fourier transform and the Hilbert transform are taken in space. However, a similar final result would be obtained if the temporal direction were taken.

The spatial HPOD problem over an infinite spatial interval is given by

$$\int_{-\infty}^{\infty}\tilde{C}(x,x',t,t')\boldsymbol{w}(x',t')\mathrm{d}x' = \sigma^2\boldsymbol{w}(x,t). \tag{44}$$

Since the target of the method is to retrieve advecting wave-packet structures, spatial wave number k and temporal frequency ω can be considered to be linked through the phase velocity $c = \omega/k$. The analytic signal of the time-space correlation tensor is then modified as

$$\tilde{C}(\xi, \tau) = \int_{-\infty}^{\infty} [1 + \mathrm{sgn}(k)] S(k, \omega) e^{ik(\xi - c\tau)} \mathrm{d}k. \tag{45}$$

Substituting $\tilde{C}$ in Eq. (44) yields

$$\int_{-\infty}^{\infty} \left[\int_{-\infty}^{\infty} [1 + \mathrm{sgn}(k)] S(k, \omega) e^{ik(\xi - c\tau)} \mathrm{d}k \right] \boldsymbol{w}(x', t') \mathrm{d}x' = \sigma^2 \boldsymbol{w}(x, t). \tag{46}$$

After some manipulation, the equation can be rewritten as

$$\int_{-\infty}^{\infty} [1 + \mathrm{sgn}(k)] S(k, \omega) e^{ik(x - ct)} \left[\int_{-\infty}^{\infty} \boldsymbol{w}(x', t') e^{-ik(x' - ct')} \mathrm{d}x' \right] \mathrm{d}k = \sigma^2 \boldsymbol{w}(x, t). \tag{47}$$

To understand the term in the square brackets of Eq. (47), $\boldsymbol{w}$ may be considered as a wave packet, i.e., to be a solution of the wave equation

$$\frac{\partial^2}{\partial t^2} \boldsymbol{w} - c^2 \frac{\partial^2}{\partial x^2} \boldsymbol{w} = 0. \tag{48}$$

The solution $\boldsymbol{w}$ at a generic time t' is linked to the solution $\boldsymbol{w_0}$ at time $t' = 0$ according to

$$\boldsymbol{w}(x', t') = \int_{-\infty}^{\infty} \mathcal{F}[\boldsymbol{w}_0](k') e^{ik'(x' - ct')} \mathrm{d}k', \tag{49}$$

where

$$\mathcal{F}[\boldsymbol{w}_0](k') = \int_{-\infty}^{\infty} \boldsymbol{w}(x', 0) e^{-ik'x'} \mathrm{d}x'. \tag{50}$$

This allows us to rewrite the term in square brackets of Eq. (47) as

$$\begin{aligned}
\int_{-\infty}^{\infty} \boldsymbol{w}(x', t') e^{-ik(x' - ct')} \mathrm{d}x' &= \int_{-\infty}^{\infty} \left[\int_{-\infty}^{\infty} \mathcal{F}[\boldsymbol{w}_0](k') e^{ik'(x' - ct')} \mathrm{d}k' \right] e^{-ik(x' - ct')} \mathrm{d}x', \\
&= \int_{-\infty}^{\infty} \mathcal{F}[\boldsymbol{w}_0](k') e^{-i(k' - k)ct'} \left[\int_{-\infty}^{\infty} e^{i(k' - k)x'} \mathrm{d}x' \right] \mathrm{d}k', \\
&= \int_{-\infty}^{\infty} \mathcal{F}[\boldsymbol{w}_0](k') e^{-i(k' - k)ct'} \delta(k' - k) \mathrm{d}k', \\
&= \mathcal{F}[\boldsymbol{w}_0](k) = \mathcal{F}[\boldsymbol{w}](k, \omega = ck),
\end{aligned} \tag{51}$$

where the last equality serves as a reminder that the generic time solution at each wave number k evolves according to a frequency ω determined by c. This result, substituted in Eq. (47), gives

$$\int_{-\infty}^{\infty} S(k, \omega) e^{ik(x - ct)} \mathcal{F}[\tilde{\boldsymbol{w}}](k, \omega) \mathrm{d}k = \sigma^2 \boldsymbol{w}(x, t). \tag{52}$$

The eigenfunction and the Fourier transform of its analytic signal can be assumed to be

$$\boldsymbol{w}(x, t) = \boldsymbol{q}(k', \omega') e^{ik'(x - c't)}, \quad \mathcal{F}[\tilde{\boldsymbol{w}}](k, \omega) = \boldsymbol{q}(k', \omega') [1 + \mathrm{sgn}(k')] \delta(k - k') \delta(ck - \omega'). \tag{53}$$

Substituting it into the eigenproblem leads to

$$\int_{-\infty}^{\infty} S(k, \omega) e^{ik(x - ct)} \boldsymbol{q}(k', \omega') [1 + \mathrm{sgn}(k')] \delta(k - k') \delta(ck - \omega') \mathrm{d}k = \sigma^2 \boldsymbol{q}(k, \omega) e^{ik(x - ct)}, \tag{54}$$

which finally results in the SPOD eigenproblem for positive k and $\omega/k = c$, i.e.,

$$S(k,\omega)\boldsymbol{q}(k,\omega)e^{ik(x-ct)} = \frac{\sigma^2}{2}\boldsymbol{q}(k,\omega)e^{ik(x-ct)}. \tag{55}$$

A similar result would be obtained if in Eq. (42) the temporal direction had been taken, with the main difference being that the solved eigenproblem would account for positive ω. It is important to highlight that the choice of computing the analytic signal in space or time does not impact on the traveling direction of the wave, which is expressed by the sign of c. In essence, considering the four quadrants in an ω-k plane, the conventional HPOD would provide modes occupying quadrants I and IV ($\omega > 0$); conversely, space-only HPOD ($k > 0$) would provide modes occupying quadrants I and II. Since backward traveling waves ($c > 0$) would symmetrically occupy quadrants II and IV, while forward traveling waves ($c < 0$) would occupy quadrants I and III, both versions of the HPOD can identify waves traveling in both directions.

Equation (55) shows that a wave-packet structure can be recognized by properly enforcing translational symmetry to the problem through the Hilbert transform either in space or time, at least while a phase velocity relation is in place. This implies that, while translational symmetry can be applied, both the conventional and space-only HPOD approaches are equivalent and would be able to retrieve wave packets. Notice that the presence of the integral operator in the dimension in which the Hilbert/Fourier transforms are computed, requires that such a dimension is resolved with high enough resolution. In the case of space-only HPOD, this means that the method works while the spatial resolution is sufficiently fine to capture the displacement of the wave with enough precision according to the phase velocity. A similar condition would be applied in the temporal resolution when the conventional HPOD problem were solved.

Also, notice that the SPOD problem in Eq. (55) has been derived assuming both stationary and homogeneous flow (which the HPOD do not necessarily require), and assuming a relation between temporal frequency and spatial wave number of a wave packet through the phase velocity. In this sense, the SPOD analysis is limited by the necessity of having a homogeneous/stationary direction in which Fourier transform can be applied. While stationarity in time is oftentimes a reasonable assumption, homogeneity along a given direction is much less common, limiting the applicability of SPOD to time-resolved sequences. In cases where homogeneity (or stationarity) cannot be assumed, a space/wave-number (or time/frequency) method should be applied in order to instate the correct symmetries. In this sense, HPOD provides a more suitable approach, which—while not guaranteeing spectrally pure modes—allows the inclusion of modulations on top of a simpler sinusoidal waveform with the analytic signal representation—largely exploited for nonstationary signal analyses. The demonstration of the equivalence between the HPOD approaches can be easily extended to cases in which the homogeneous/stationary flow assumptions drop and the HPODs do not converge to the SPOD problem anymore. It is worth highlighting that the equivalence of the two HPOD approaches only holds for advecting features, i.e., when a phase velocity relation is in place between temporal frequency and spatial wave number. For phenomena of different nature, the two approaches should not be expected to converge to the same solution, while still retaining the analytic signal nature of either temporal and spatial patterns. This, however, should not be considered a detrimental aspect of the space-only approach versus the conventional approach, but rather a feature that can be exploited, for example to target more effectively advecting features and rule out other time-dependent phenomena, thus justifying the use of the space-only HPOD also in scenarios where temporal resolution is available.

III. TEST CASES

This section proposes three different test cases to demonstrate the properties of the HPOD and highlight its capabilities. The datasets are proposed in order of their complexity in terms of data-driven modal analysis.

The first dataset is the velocity field of the laminar vortex shedding behind a cylinder extracted from 2D-DNS. This dataset is the least complex one, in which few flow features with a clear frequency signature are present and in which temporal resolution is available. This flow has been plenty analyzed by means of data-driven techniques—POD being a primary example—making it a perfect didactic example with a well-known and easily recognizable flow model. As such, it allows demonstrating the most basic properties of the HPOD, in particular its capability to deliver spatiotemporally coherent structures, already organized in complex-valued modes, which do not require *a posteriori* pairing as the POD ones. Moreover, its robustness to the lack of temporal resolution in the space-only implementation can be introduced.

The second dataset is the velocity field of a turbulent jet flow extracted from a LES. This dataset represents a more complex scenario than the previous one, since—despite the presence of advective flow features—a large wealth of turbulent scales is present and there is no clear frequency signature. This dataset is used to demonstrate the capabilities of the HPOD to extract advective structures also in a very challenging scenario characterized by a broadband spectral content, whereas other techniques can be subjected to mode mixing. Additionally, it allows to emphasize the analytic signal nature of the HPOD modes and its effect of their frequency/wave-number content.

Finally, the third dataset is a collection of flow field snapshots of a turbulent jet measured with planar PIV. This dataset provides similar challenges with respect to the previous case in terms of turbulence scales and broadband spectral content, adding on top of it measurement uncertainty and temporally unresolved data. This last dataset is intended as a proof of concept for the practical application of the space-only HPOD for retrieving spatial modes interpretable as advective flow structures (similar to the ones obtained in the LES case) even using real data from experiments with no temporal information available.

A. DNS of a laminar vortex street in the wake of a cylinder

The conventional and space-only HPOD are tested on a numerical database obtained from the 2D-DNS of the flow around a cylinder of diameter D at $\mathrm{Re} = 100$. The flow around the cylinder has been computed through the OpenFOAM solver pimpleFoam. The dataset used in this test case includes 10 800 time-resolved snapshots spanning a cropped domain of $10.6D \times 4.8D$ corresponding to 91×201 mesh points. The temporal separation between frames corresponds to an advective time $\Delta t U_\infty / D = 0.0139$, resulting in a time-resolved sequence. This database has been selected, since the laminar vortex street in the wake of the cylinder offers a clear periodic signature, which can help clarify the potential of the space-only application of the HPOD. Additionally, since the original sequence is time-resolved, the conventional HPOD (applied in time) can be implemented, providing a point of comparison between the two distinct implementations of HPOD.

Figure 1 (left) reports the ratio of the first 10 squared singular values, representing the energy content in each *structure*, versus the total energy content of the sequence for the HPOD implementations in time and in space (along the x direction) for the original time-resolved sequence. To exemplify the implication of the edge effects described in Sec. II C, the HPOD has been applied both considering a 15% data removal at the end of each side of the analytic signal of the dataset (either along the x direction or t depending on the implementation), i.e., retaining information of 70% of the sequence, as well as retaining the 100% of the sequence. The traditional POD has been included for comparison. The distribution of the energy shows that, in this case, both the HPOD implementations retrieve a more compact decomposition than POD, predicting only a single structure containing most of the energy, while the POD—as expected—splits the energy in the first two structures. This effect results from the removal of redundant negative frequency content operated by the analytic signal, which allows for absorbing the POD mode pairs as real and imaginary parts of the HPOD modes with identical frequency and amplitude. Additionally, the need for a reduced number of modes to reconstruct the same information can be considered beneficial also in terms of the robustness of the decomposition, allowing a stronger signal-to-noise ratio for HPOD modes. Discrepancies between the two implementations can be observed only for low-energy structures and

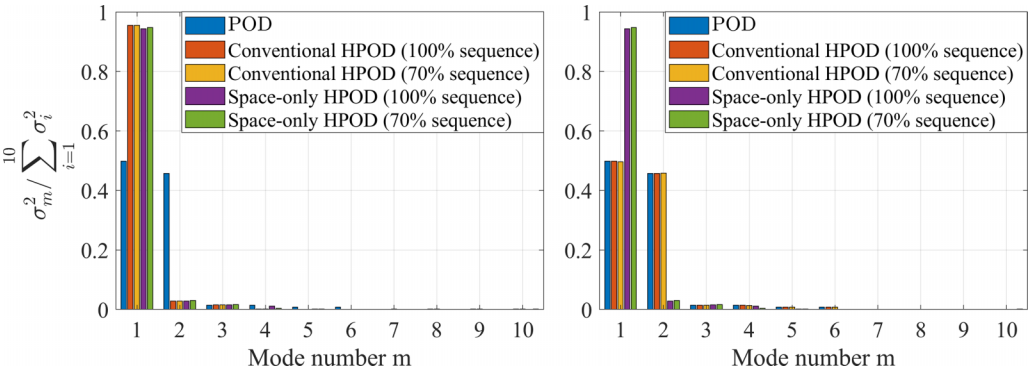

FIG. 1. Energy content of each mode vs the total energy content of the sequence for the HPOD implementations and POD: (left) original time-resolved sequence; (right) sequence shuffled in time.

they are typically negligible. The distribution of energy seems to be even less altered when part of the sequence is filtered out. Fig. 1 (right) reports the same energy content distribution computed for the time-resolved sequence being shuffled, i.e., the original order of the snapshot in the original time sequence has been randomly changed, to mimic non-time-resolved data. As expected, while the space-only HPOD retain the same energy distribution as in the unshuffled case, the conventional implementation in time cannot correctly complexify the sequence, converging, therefore, towards the standard POD. This phenomenon has already been reported by Kriegseis *et al*. [26]. So far, the differences between the decompositions have been highlighted from an energy point of view. In the following, the difference will be highlighted in terms of temporal and spatial patterns and a deeper insight will be given for both edge effects and the lack of temporal resolution.

1. Mode comparison: POD versus conventional HPOD versus space-only HPOD

While the distribution of energy and the compactness of the decomposition are relevant features, the main interest in this test case is to show the capabilities of HPOD to retrieve advective flow structures. In this sense, the wake behind a cylinder is a perfect test case for didactic purposes: the vortex street is represented by traveling waves of vorticity propagating in the flow direction with little to no temporal modulation. For simple flow scenarios not affected by mode mixing, the standard POD, as most of the readers had already experienced, identify for each wave a pair of modes sharing a quadrature phase relation both in space and time. These modes can be paired *a posteriori* as real and imaginary parts of an oscillatory model, which represent the benchmark against which the HPOD should be compared. Figure 2 reports the first three *structures* retrieved by the conventional implementation of the HPOD in time (second column, referred to as $\mathrm{HPOD_t}$ in here) and for the space-only implementation of the HPOD in the advection direction x (third column, referred to as $\mathrm{HPOD_x}$ in here) for the time-resolved original sequence without data removal (100% of the data). The complex-valued spatial modes are reported in terms of their real and imaginary parts. The first six spatial modes of the POD, grouped in pairs, are reported for comparison in the first column. The fourth column reports the temporal mode of the HPOD implementations and of the POD mode pairs in the form of a phase plot (real versus imaginary part for the HPOD and cyclogram between paired modes for the POD). The spatial modes retrieved by the two HPOD implementations look extremely similar in amplitude and wavelength in the x direction, differing only for being in phase opposition, as shown by the discrepancy in their imaginary part. This seeming discrepancy, however, is by construction and does not affect the physical behavior of the retrieved structures, as will be fully clarified for the next testcase. The retrieved complex-valued spatial modes correspond to mode pairs of the POD, which clearly represent pairs of modes in phase quadrature in space. In terms of phase plots of temporal modes, the POD, as expected for a von Kármán street, retrieves

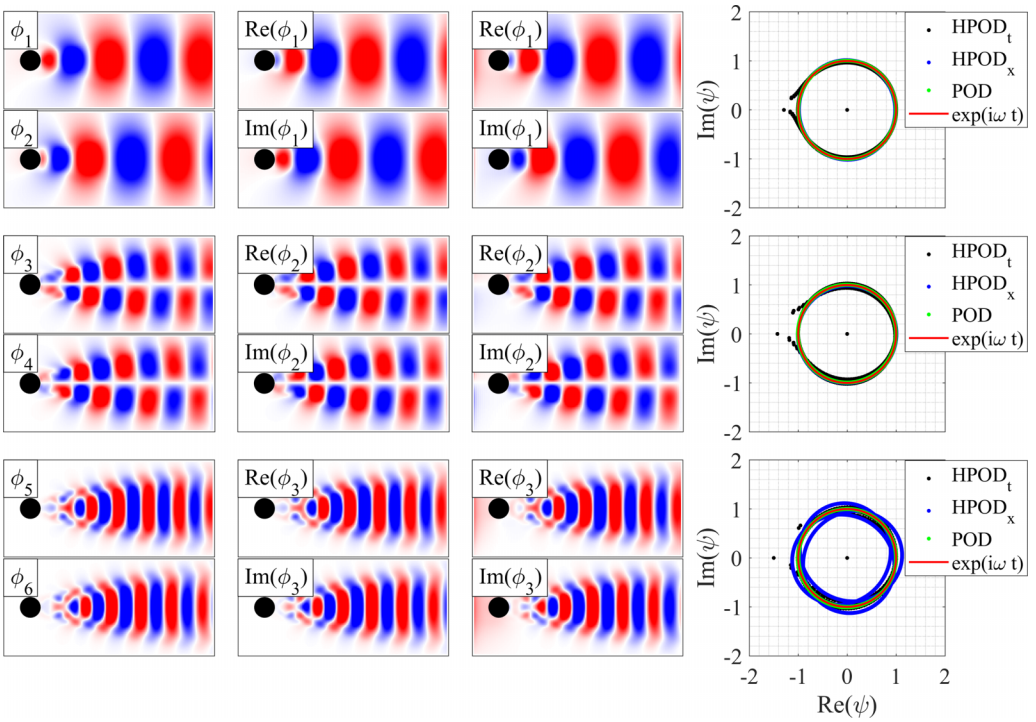

FIG. 2. Comparison between POD and HPOD modes—computed on the original time-resolved sequence, 100% of the sequence: first three pairs of spatial POD modes (first column); first three spatial modes of the conventional HPOD (second column); first three spatial modes of the space-only HPOD (third column); phase plot of the temporal modes for HPOD implementations and for POD pairs (fourth column).

mode pairs, which behave temporally as pure sinusoid with a phase shift of $\pi/2$: each temporal mode pair, represented as the real and imaginary parts of a single complex-valued mode, form a Lissajous figure corresponding to the unitary circle $\exp(i\omega t)$, represented in red in the plots. The complex-valued temporal modes from the HPODs tend to follow the same unitary circle, which is compatible with spectrally pure modes in time. While the HPODs seems to recover the general behavior of POD mode pairs, it is possible to observe some important discrepancies both in the spatial and temporal patterns. Particularly for the latters, the temporal patterns of the first two modes show a departure from the unitary circle at the edges of the sequence in the HPOD$_t$, while for the third mode waviness appears associated to the HPOD$_x$. These discrepancies are due to edge effects from the Hilbert transform, which will be discussed in the following.

2. Impact of edge effects on modes purity

Figure 3 reports the first three *structures* retrieved by the conventional HPOD (second column) and for the space-only HPOD (third column) for the time-resolved original sequence with edge removal (70% of the data). An important point needs to be highlighted when looking at the differences between full sequence (Fig. 2) and reduced sequence (Fig. 3) results: for the full sequence, distortions of the modes appear. These distortions are typically relevant in the boundary of the direction in which the Hilbert transform has been implemented (the time in the conventional implementation and the direction x in the space-only implementation), which are compatible with the edge effects of the transform. For low-energy modes, this distortion seems to propagate also into other directions, as shown for the space-only HPOD in Fig. 2, row 3, column 4, where the distortion propagates also in time indicating that the mode includes a spurious temporal modulation due to

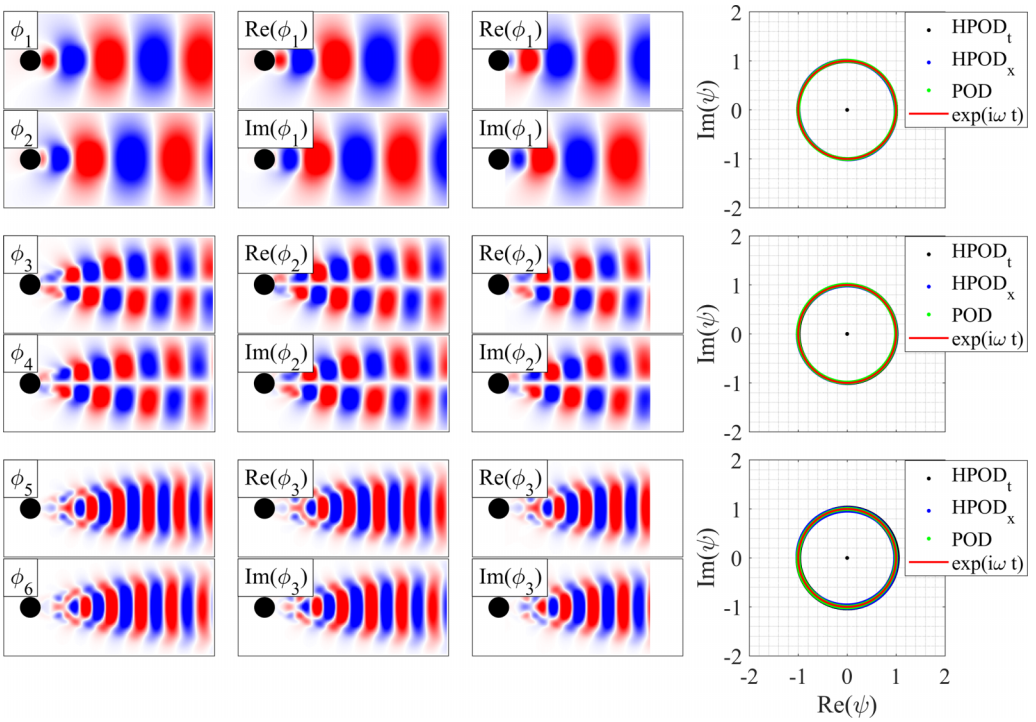

FIG. 3. Comparison between POD and HPOD modes—computed on the original time-resolved sequence, 70% of the sequence: first three pairs of spatial POD modes (first column); first three spatial modes of the conventional HPOD (second column); first three spatial modes of the space-only HPOD (third column); phase plot of the temporal modes for HPOD implementations and for POD pairs (fourth column).

the spatial edge distortion. These distortion effects seem to be completely suppressed if 15% of the signal is removed from the signal end after the Hilbert transform. Obviously, this signal reduction is reflected in the reduction of the domain in which the mode is retrieved, which in the space-only implementation results in a shrinkage of the spatial domain in the x direction. It must be remarked that this 15% signal reduction has been selected on an empirical basis as a conservative measure to ensure edge effects are removed completely. An accurate treatment of Hilbert transform edge effect is outside the scope of the present work. Less conservative criteria, or even other edge-effect treatment techniques, can be implemented to reduce shrinkage of the signal, as already mentioned in Sec. II C. A full discussion on the edge-effect treatment is an issue regarding the optimization of the numerical implementation of the HPOD, which is beyond the purpose of the present paper.

3. Effect of temporal undersampling

The HPOD is repeated for the temporally shuffled sequence of velocity fields in order to simulate a non-time-resolved dataset. This has been performed by randomly permuting the order of the snapshots in the time-resolved sequence, thus removing the order relation between them to achieve a virtually undersampled sequence. Figures 4 and 5 shows the first three *structures* retrieved by the conventional and space-only implementations of HPOD respectively, without data removal (100% of the sequence, Fig. 4) and with data removal (70% of the sequence, Fig. 5). As expected, the space-only HPOD$_x$ is unaffected by the sequence not being time-resolved and still provides results that match the standard POD pairs both in terms of spatial and temporal modes. The conventional HPOD$_t$, instead, cannot properly complexify the dataset due to the lack of resolution in the temporal direction. The modes it retrieves are, therefore, converging towards POD modes both in terms of

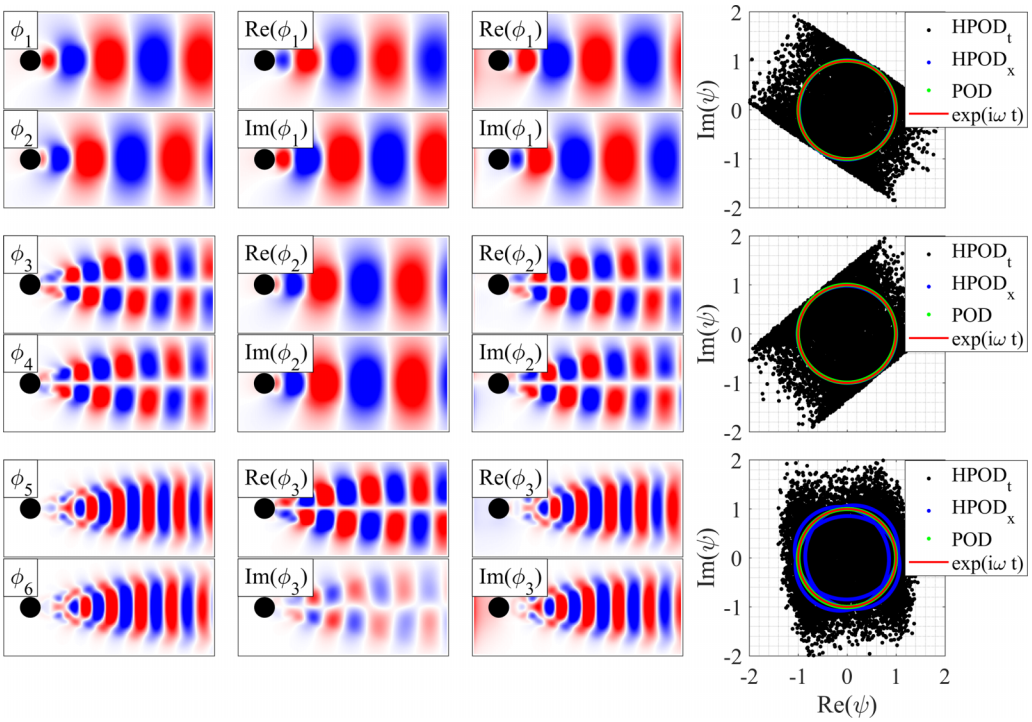

FIG. 4. Comparison between POD and HPOD modes—computed on the shuffled sequence, 100% of the sequence: first three pairs of spatial POD modes (first column); first three spatial modes of the conventional HPOD (second column); first three spatial modes of the space-only HPOD (third column); phase plot of the temporal modes for HPOD implementations and for POD pairs (fourth column).

space and time. This is evident by the fact that each complex-valued temporal mode does not show a clear quadrature phase relation between its real and imaginary parts, as in the previous case. Also, spatial modes with the same spatial frequency content appear, i.e., mode pairs as in the POD approach, showing that HPOD$_t$ is not capable of recognizing them as part of a single complex-valued mode, but rather a retroactive pairing is needed to recover the spatiotemporal behavior. It is worth highlighting that despite the fact that the modes tend to converge towards the POD ones, they retain their complex-valued nature, having a non-null imaginary part—however, without a physically sound meaning.

B. LES of a turbulent jet

The performances of the conventional and space-only HPOD are further tested in a more complex scenario, characterized by a broadband spectral content but still dominated by advecting flow structures. A velocity field database has been extracted from the high-fidelity LES of a turbulent jet at $M = U_j/a = 0.9$ and $\mathrm{Re}_j = U_j D/\nu \approx 10^6$ provided by Towne *et al.* [58]. This flow is characterized by traveling wave packets forming in the shear layer—as shown through SPOD analysis by Towne *et al.* [58]—which are not shed at a fixed frequency but rather possess a broadband spectrum. The eduction of coherent features in the form of wave packets is a topic of particular interest in the turbulent jet noise community: their correct modeling is central in the effort to provide better estimation of the sound emission [6]. This dataset allows us to demonstrate the capability of HPOD to retrieve spatiotemporally coherent features characterized by modulation (and intermittency) both in space and time, and thus profoundly differing from spectrally pure SPOD modes. Differently

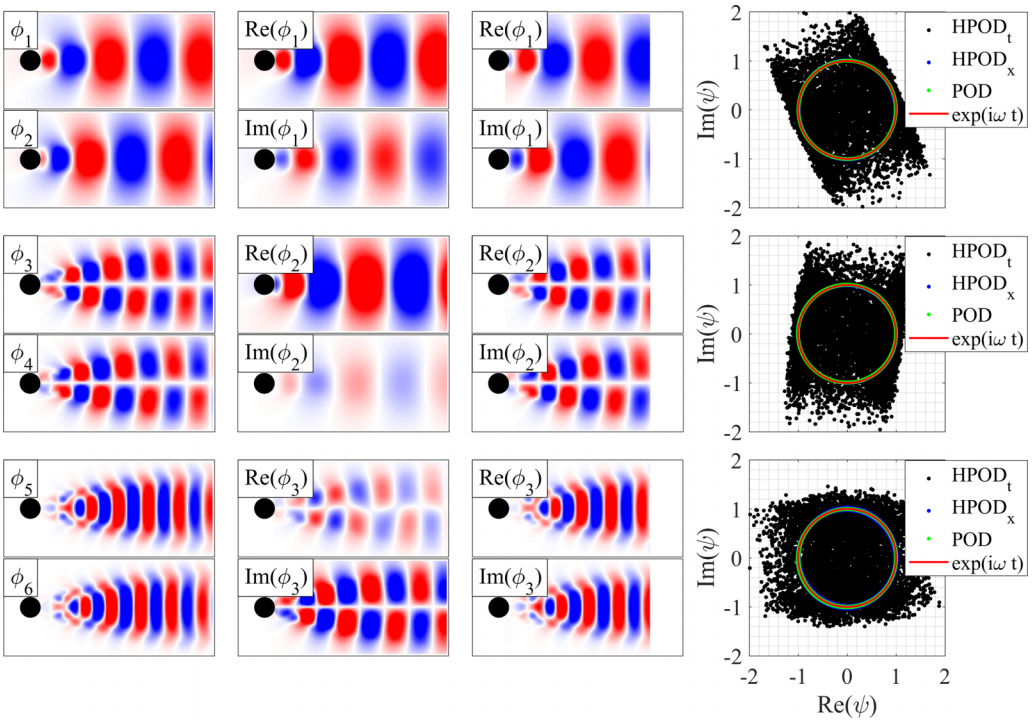

FIG. 5. Comparison between POD and HPOD modes – computed on the shuffled sequence, 70% of the sequence: first three pairs of spatial POD modes (first column); first three spatial modes of the conventional HPOD (second column); first three spatial modes of the space-only HPOD (third column); phase plot of the temporal modes for HPOD implementations and for POD pairs (fourth column).

from the previous case, the complexity of the flow under analysis does not allow the application of space-only POD: while it is not shown explicitly in the following, the POD of this flow is heavily affected by mode mixing, making impossible to retrieve matching pairs of modes corresponding to spatiotemporally coherent features. This is likely due to both the large wealth of scales involved in this flow, as well as to the presence of modulation and intermittency effects. As will be shown in the following, by not imposing stationarity like in SPOD, the HPOD allows to capture the intermittency of spatiotemporally coherent flow features (which would also tend to emerge in POD despite the mode mixing).

The database is constituted by 10 000 time-resolved snapshots sampled at $\Delta t = 0.2D/a$, where a is the speed of sound and D is the nozzle diameter. The data are available over a structured cylindrical grid spanning 30 D in the axial direction and 6 D in the radial one, containing 656, 138, and 128 points in the axial, radial, and azimuthal directions, respectively. For the application of the HPOD, a single plane at a fixed azimuthal coordinate has been extracted for each snapshot. In the following, the velocity field including the axial and radial components in this plane will be considered. While the choice of variable to identify wave packets in jet noise cases typically falls on the hydrodynamic pressure field, the velocity field has been chosen in this case in order to provide a more direct connection to the jet velocimetry data analyzed in the third testcase.

The conventional HPOD applied in the temporal direction has been compared to the space-only HPOD performed along the axial direction. To provide a fair comparison, 15% of the data at each end of the signal in both the temporal and spatial directions have been removed. The first three complex-valued structures computed with both approaches are presented in Figs. 6 and 7, respectively. These structures correspond to approximately 8.1%, 7.2%, and 6.0% of the turbulent

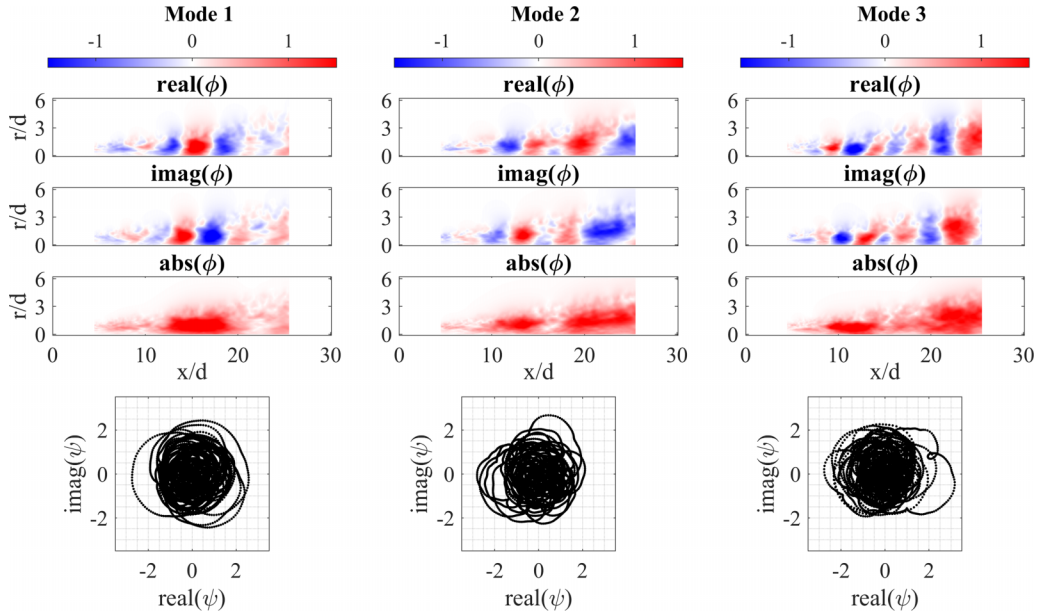

FIG. 6. Radial velocity component of the complex-valued spatial modes of the HPOD performed in the temporal direction: (left) first mode, (center) second mode, (right) third mode. From top to bottom: real part of the spatial mode; imaginary part of the spatial mode; absolute value of the spatial mode; phase plot of the real vs imaginary part of the temporal mode.

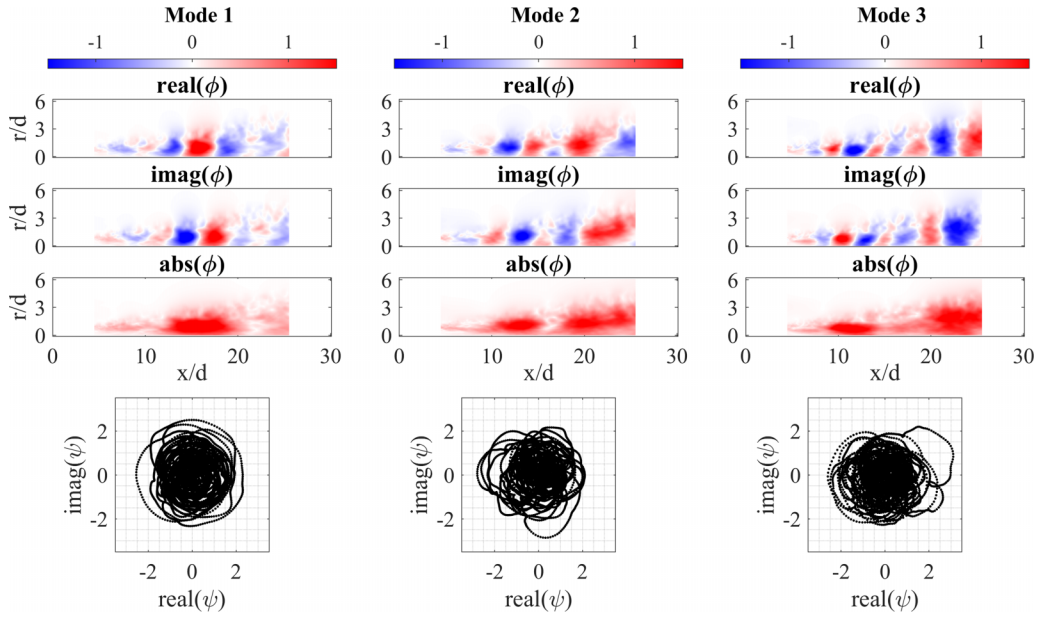

FIG. 7. Radial velocity component of the complex-valued spatial modes of the HPOD performed in the advective direction: (left) first mode, (center) second mode, (right) third mode. From top to bottom: real part of the spatial mode; imaginary part of the spatial mode; absolute value of the spatial mode; phase plot of the real vs imaginary part of the temporal mode.

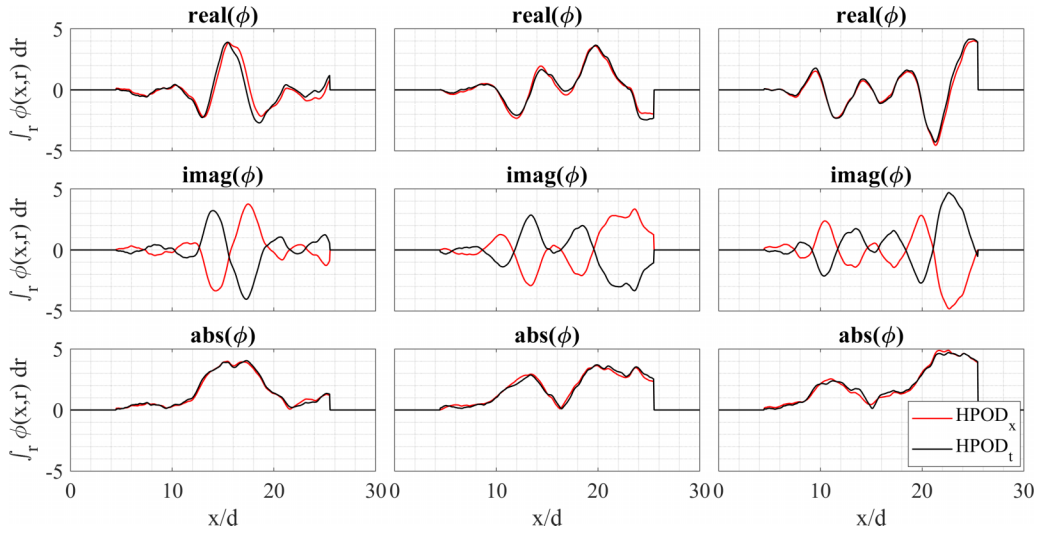

FIG. 8. Radial integral of the radial velocity component of the complex-valued spatial modes of the HPOD.

kinetic energy contained in the dataset for the conventional HPOD and to approximately 8.4%, 7.5%, and 6.2% for the space-only HPOD. Given their complex-valued nature, the spatial modes have been represented with their real (first row), imaginary (second row) and absolute (third row) values, while temporal modes have been represented as a phase plot of the real value versus the imaginary value (fourth row). Both the HPOD applied in time and in space show similar spatial modes for corresponding structures, i.e., a wave packet structure with similar spatial frequency content, where the real and imaginary components are shifted by $\pi/2$ in the advection direction. The main difference between the patterns of the HPOD performed in time and space is the phase of the modes. For example, the real part of the first mode is almost identical, while the imaginary part has opposite signs, suggesting that the modes are in phase opposition. Similar behaviors can be observed also for the second and third modes, showing that the spatial modes delivered by the space-only HPOD are approximately the complex conjugate of the spatial modes delivered by the conventional HPOD (manifesting itself as a π shift in the complex-valued mode). The intensity of the flow field wave-like oscillations exhibit an almost identical modulation along the streamwise direction, which can be better appreciated from the absolute value of the mode. In particular, the first mode shows a distributed peak between $x/d = 10$ and 20, the second mode shows two peaks at about $x/d = 13$ and 21, while the third mode shows two peaks at $x/d \approx 12$ and $x/d \approx 23$. A similar modulation pattern is also observable on the SPOD modes recovered by Towne *et al.* [22] for a turbulent jet at $M = 0.4$.

To further highlight the wave packet nature of the spatial patterns extracted through HPOD and provide a more clear overview of the similarity of the results provided by the conventional and space-only implementation, Fig. 8 presents the line plots obtained by integrating the spatial patterns in the radial direction. The extracted waveforms clearly show that both HPOD implementation delivers practically the same waveforms, with the only difference being the phase opposition in their imaginary part, as it has already been observed above.

The phase plots of the temporal modes reported in the fourth row of Figs. 6 and 7 show that the retrieved jet modes do not distribute around a unitary circle $\exp(i\omega t)$. This means that these modes are not spectrally pure, differently from what was observed for the cylinder wake, but are instead characterized by modulation in both amplitude and frequency. To have a better insight into the behavior of these temporal modes, a time-frequency analysis is proposed in Figs. 9 and 10. The spectrograms have been computed through windowing the signal with rectangular windows with

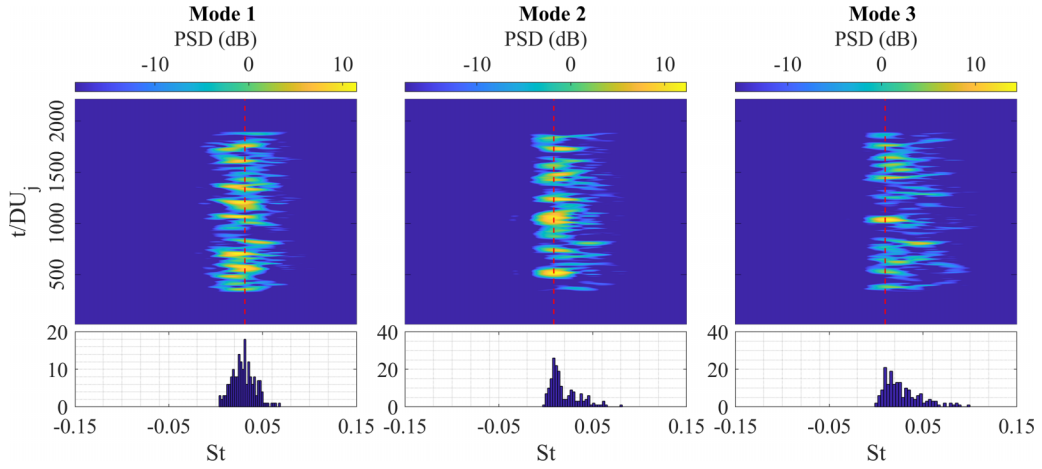

FIG. 9. Spectrogram of the complex-valued temporal modes of the HPOD performed in the temporal direction (top) and histogram of the peak frequency through time (bottom). From left to right: (left) first mode, (center) second mode, (right) third mode.

75% overlap to obtain 248 signal segments with equal span centered at different instants. Short-time Fourier transform has been computed on each signal segment to provide its frequency content at a given instant. The values of the power spectral density (PSD) are plotted in a scale spanning 30 dB from the maximum value. Notice that, due to the complex-valued nature of the modes, the power spectrum is not even, i.e., symmetric with respect to the zero frequency. It is worth highlighting that these modes have either the negative- or the positive-frequency side of the spectrum equal to zero. This behavior confirms that the modes are analytic in nature.

The time-frequency analysis reveals that the spectral content of these modes varies with time but appears band-limited in frequency. The temporal modes alternate instants in which (i) the mode is active and its spectral content peaks at a given frequency, and instants in which (ii) the spectral content goes to zero, i.e., the mode is inactive. This behavior indicates that the retrieved modes are

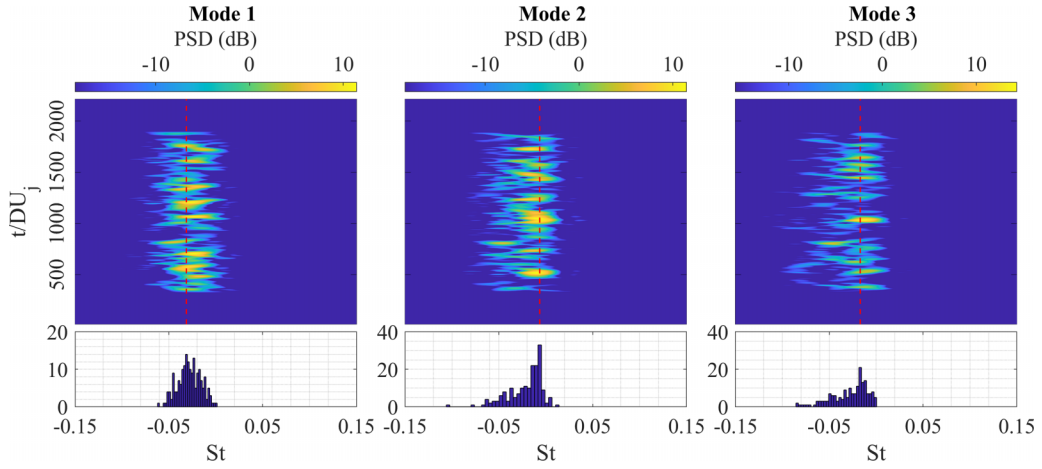

FIG. 10. Spectrogram of the complex-valued temporal modes of the HPOD performed in the advective direction (top) and histogram of the peak frequency through time (bottom). From left to right: (left) first mode, (center) second mode, (right) third mode.

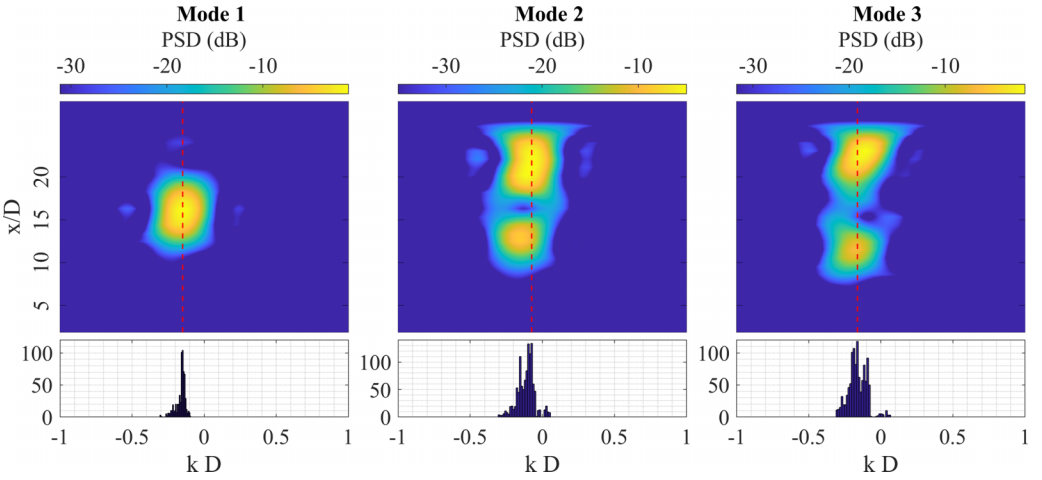

FIG. 11. Spectrogram along x of the complex-valued spatial modes of the conventional HPOD (top) and histogram of the peak spatial wave number through the advective direction (bottom). From left to right: (left) first mode, (center) second mode, (right) third mode.

intermittent. Apart from the modulation in amplitude, showing different energy content in time, the temporal modes are also affected by a modulation in frequency, with slight shifts of the frequency content through time. To further stress this point, the histogram of the peak frequency in each temporal window analyzed in the spectrogram is reported. Despite the fact that the peak frequency changes through time, statistically it seems to distribute around a specific frequency around which the mode is modulated in frequency.

A similar space-wave-number analysis is performed on the spatial modes delivered by the conventional and space-only HPOD in Figs. 11 and 12. Rows along x of the vector field have been extracted to obtain a signal for each radial position r. For each signal, the spectrograms have been computed through windowing with rectangular windows with 75% overlap to obtain 29 signal

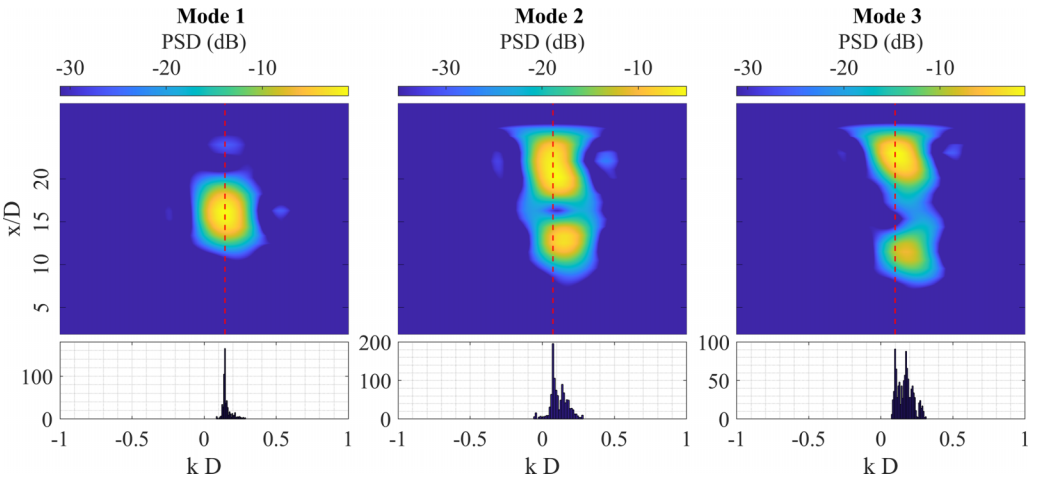

FIG. 12. Spectrogram along x of the complex-valued temporal modes of the space-only HPOD (top) and histogram of the peak spatial wave number through the advective direction (bottom). From left to right: (left) first mode, (center) second mode, (right) third mode.

segments with equal span centered at different x positions. Short-time Fourier transform has been computed on each signal segment to provide its frequency content at a given spatial location. The values of the PSD averaged along the radial position are plotted in a scale spanning 30 dB from the maximum value. Similarly to the temporal modes, also spatial modes have either the negative- or the positive-wave-number side of the spectrum equal to zero. This behavior confirms that the spatial patterns as well are analytic in nature. Additionally, also the spatial wave number content of the spatial patterns is band-limited, even if characterized by modulation in amplitude and wave number depending on the axial position. This is better visualized through the histogram of the peak wave number in each spatial location (in both x and r), which reveals a distribution around a specific spatial wave number around which the mode shows a more or less strong modulation in wave number. As the mode number is increased, this peak wave-number value is shown to increase. This behavior is to be expected, since typically large scale flow structures carry higher kinetic energy, and thus will be ranked first by the HPOD.

It is worth highlighting that the spectrograms of the temporal and spatial modes computed by both the conventional and space-only HPOD are almost perfectly symmetric with respect to the zero frequency/wave number, showing almost the same spectral content apart from the sign. In particular, the temporal spectral content for the conventional HPOD only occupies the positive-frequency side, while for the space-only HPOD occupies the negative-frequency side. The spatial spectral content, instead, provides only negative wave numbers for the conventional HPOD, while for the space-only HPOD it provides only positive wave numbers. This means that the two implementations of the HPOD deliver temporal and spatial modes, which are approximately the same apart from being one the complex conjugate of the other.

This behavior can be explained by both the properties of the Hilbert transform (used to compute the analytic representation of the field) and the relation between the temporal frequency and spatial wave number provided by the phase velocity. The Hilbert transform operation used to complexify the flow field forces the negative side of the spectrum to zero in the direction in which the Hilbert transform is performed, i.e., for the conventional HPOD performed in time the negative temporal frequency will be zero while for the space-only HPOD performed in space the negative spatial wavelengths will be zero. Since temporal frequency and spatial wave number for an advective wave are linked through the phase velocity as $c = \omega/\lambda$, for advective waves moving towards positive x direction, i.e., characterized by negative phase velocities, the temporal frequency of the space-only HPOD has to be negative to compensate for the positive spatial wave number. Similarly, the conventional HPOD needs to have negative wave numbers, which manifest as a phase opposition in the spatial patterns with respect to the space-only HPOD, characterized instead by positive wave numbers. Notice that, both spatial and temporal modes delivered by the conventional and space-only HPOD are one the complex conjugate of the other. That is, when the spatiotemporal structure is assembled from these modes it behaves in the same physical way, making the two approaches equivalent for purely-advecting features.

As a final remark, we test the capability of the space-only HPOD to provide a virtually identical decomposition of complex advection-dominated flows even when no temporal resolution is available. Figures 13 and 14 shows the results, respectively, of the conventional and space-only HPOD when applied to the shuffled time-series (replicating the same test performed for the cylinder wake in Sec. III A). While the space-only HPOD would still be able to provide the correct complex-valued representation, with real and imaginary parts of the modes being in phase quadrature and showing the same characteristics as the mode extracted from the time-resolved sequence, the conventional HPOD loses this capability, converging towards modes not representing the complex exponential of a wave packet.

C. Turbulent jet experiment

As has been shown so far, both the conventional and space-only HPOD approaches are capable of delivering modes, which can represent advecting features in the form of wave packets. In most experimental settings, however, obtaining flow field data with enough temporal resolution to identify

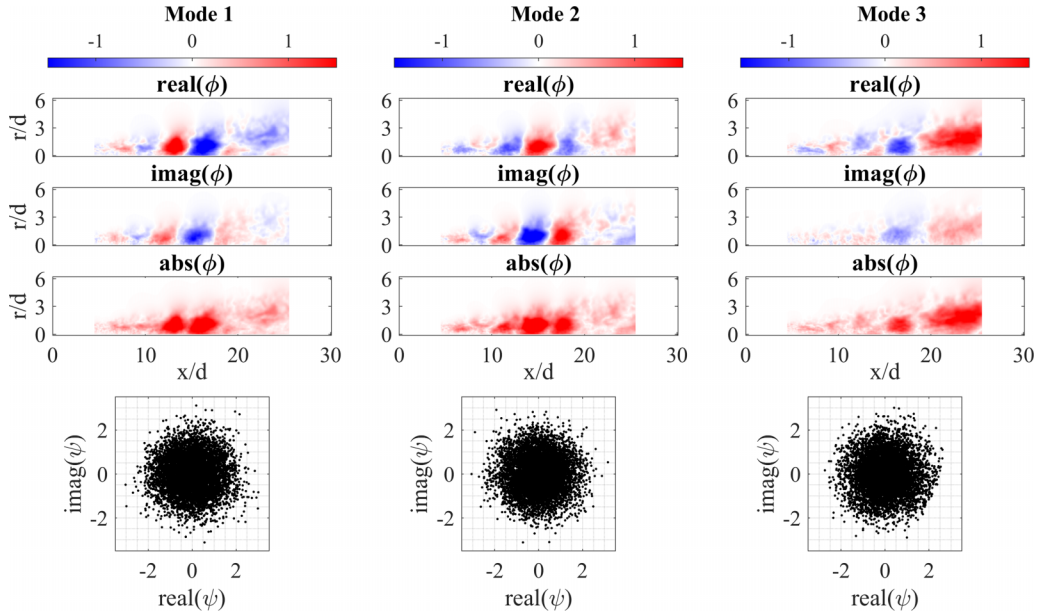

FIG. 13. Radial velocity component of the complex-valued spatial modes of the conventional HPOD for the shuffled sequence: (left) first mode, (center) second mode, (right) third mode. From top to bottom: real part of the spatial mode; imaginary part of the spatial mode; absolute value of the spatial mode; phase plot of the real vs imaginary part of the temporal mode.

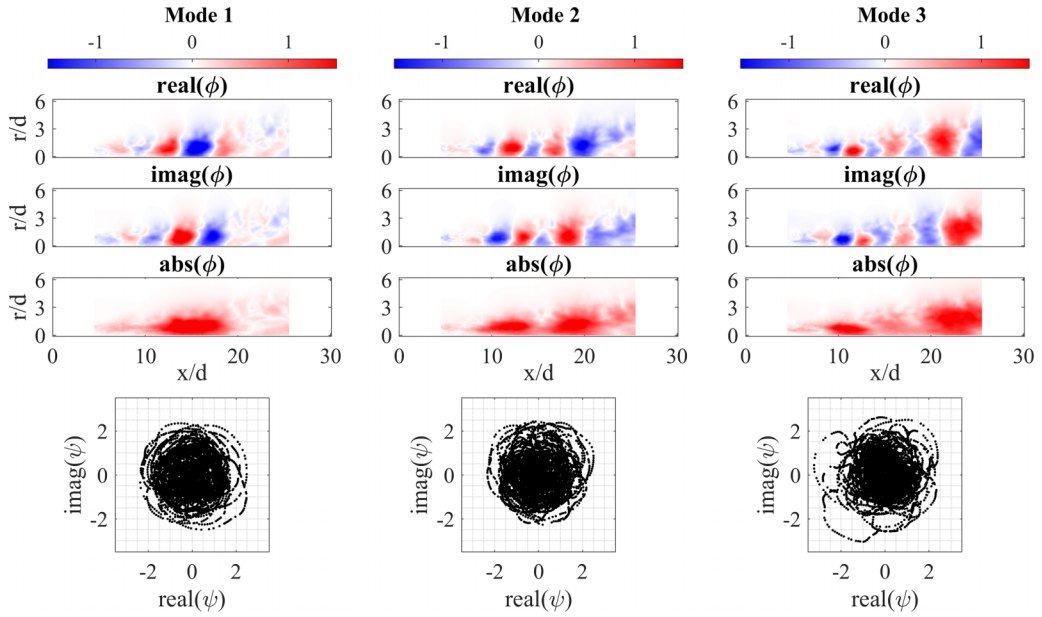

FIG. 14. Radial velocity component of the complex-valued spatial modes of the space-only HPOD for the shuffled sequence: (left) first mode, (center) second mode, (right) third mode. From top to bottom: real part of the spatial mode; imaginary part of the spatial mode; absolute value of the spatial mode; phase plot of the real vs imaginary part of the temporal mode.

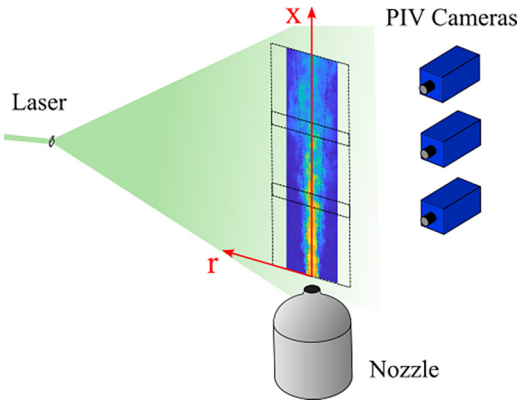

FIG. 15. A sketch of the turbulent-jet experimental setup.

the underlying flow dynamics can be challenging. This lack of data rules out the application of the conventional HPOD (as well as of other time-based data-driven decomposition techniques). Velocity field measurement techniques, however, provide instead enough spatial resolution to solve the wave displacement in the advection direction: this opens the way for the use of space-only HPOD to extract advecting features from the data, even with the lack of the dynamics information. To prove the suitability of this approach, the method is tested on snapshot PIV data from a turbulent subsonic jet experiment described by Raiola and Ragni [59]. The jet issues from an axial-symmetric nozzle with exit diameter $D = 20$ mm with a jet exit velocity $V_J = 25$ m/s, resulting in a Reynolds number of $\mathrm{Re} = V_J D/\nu = 33\,000$. Planar PIV is used to measure flow fields in the symmetry plane of the jet. Proper jet seeding is obtained by feeding into the stagnation chamber air premixed with DEHS droplets (with approximately 1 μm diameter) produced with a Laskin nozzle. The jet is confined in a closed structure with approximate dimensions $50D \times 50D \times 50D$ in order to have similar particle concentration inside and outside the jet. A double-pulsed Quantel Evergreen Nd:Yag Laser (200 mJ/pulse at 15 Hz) is used to illuminate a plane passing through the symmetry axis of the jet. A set of three sCMOS Andor Zyla 5.5Mpixels cameras aligned along the jet axis direction is employed to image the flow field, spanning a field of view of $6D \times 20D$. A sketch of the experimental setup is provided in Fig. 15. The particle images have been cross-correlated using a multipass image deformation algorithm. The final interrogation region size is 40×40 pixels with 75% overlap, corresponding to a vector spacing of $0.029D$ in the velocity fields measured. The final ensemble consists of 2600 velocity fields sampled at 10 Hz repetition rate. In the present analysis, only half of the entire domain with respect to the jet centerline has been considered. This choice helps in preserving the circular symmetry of the problem and to avoid polluting the modes with information from the homogeneous azimuthal direction.

The first three complex-valued structures obtained from the decomposition are depicted in Fig. 16. These modes correspond to 8.8%, 6.7%, and 5.4% of the turbulent kinetic energy contained in the dataset, respectively. The complex-valued spatial modes ϕ are depicted both in their real and imaginary values in the first two rows. For each mode real and imaginary part have the same wave number content in space but shifted $\pi/2$ apart, thus indicating that they model a traveling wave packet similarly to what has been observed for the LES case. Also, as the mode order is increased, their wave number increases. The absolute value of the mode, represented on the third row, reveals that each traveling wave undergoes a spatial amplification and decay, providing a spatial modulation of the wave in the streamwise direction which resemble similar modulation patterns observed in the LES case.

The spatial spectral content of each spatial mode can be better appreciated in the space/wave number spectrograms in Fig. 17, obtained following the same procedure as for Fig. 12. The

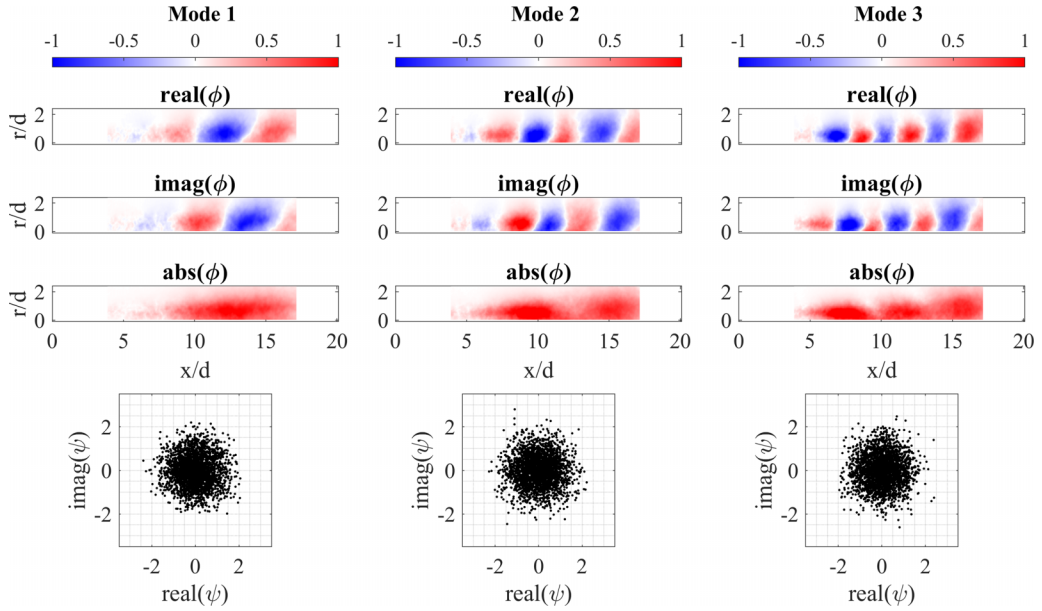

FIG. 16. Radial component of the complex-value HPOD modes: (left) first mode, (center) second mode, (right) third mode. From top to bottom: real part of the spatial mode; imaginary part of the spatial mode; absolute value of the spatial mode; phase plot of the real vs imaginary part of the temporal mode.

analysis shows that—as expected for the space-only HPOD—the spatial spectra only include the positive-wave-number side. The spectrograms for all modes are characterized by a strong modulation of the wave in amplitude and wave number along x. The spectral content is, however, quite band-limited, as already observed for the LES case: wave-number modulation happens around a most probable value, as revealed by the peak-wave-number histogram. Similarly to the LES case, this peak wave-number value tends to increase as the mode number increases, capturing modes with decreasing energy content.

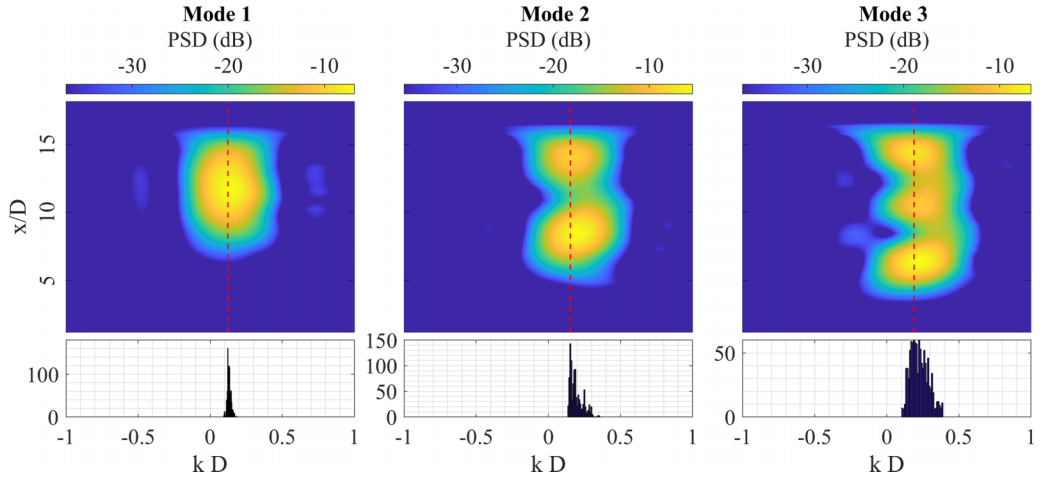

FIG. 17. Spectrogram along x of the complex-valued temporal modes of the space-only HPOD (top) and histogram of the peak spatial frequency through the advective direction (bottom). From left to right: (left) first mode, (center) second mode, (right) third mode.

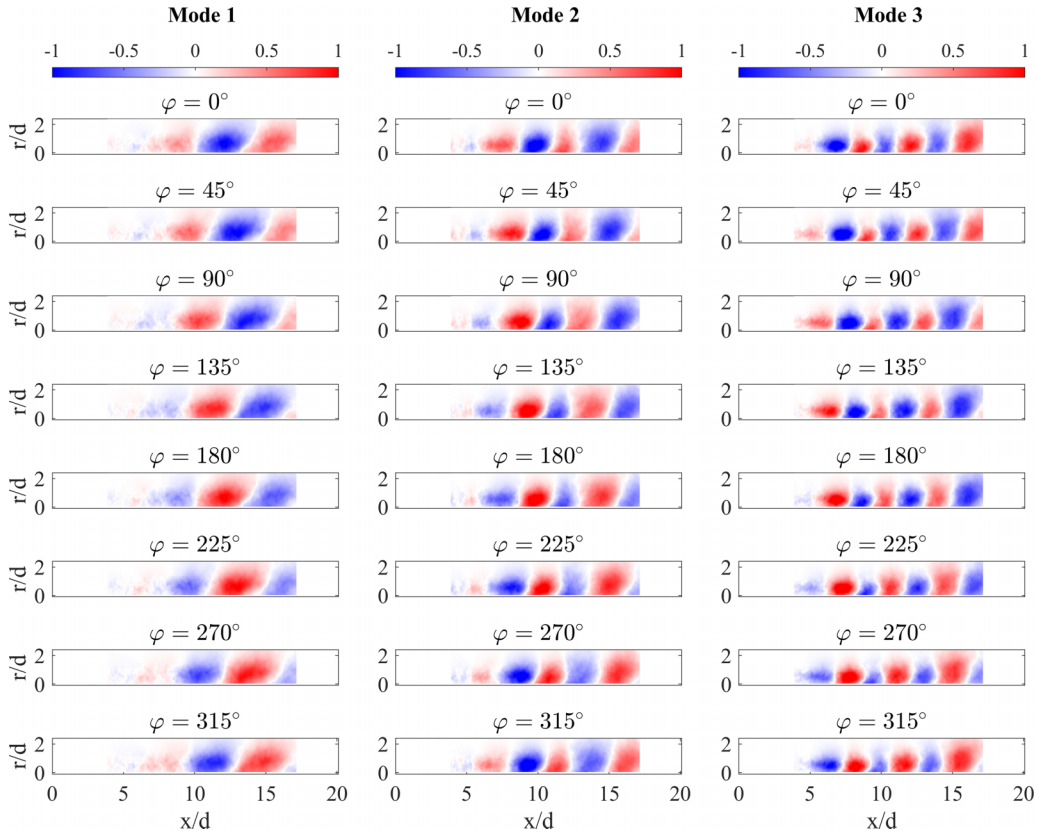

FIG. 18. Radial component of the oscillator model of the space-only HPOD modes: (left) first mode, (center) second mode, (right) third mode. From top to bottom: different phases according to the oscillator model.

Finally, cyclograms of the real versus imaginary values of each temporal mode are depicted on the fourth row of Fig. 16. No clear unitary circle or other Lissajous figure can be spotted, suggesting that, similarly to what has been observed in the LES case, the phenomenon is chaotic and dominated by modulation in time of the modes, which, for heavily undersampled data, would produce randomly filled circles in the cyclogram.

Despite the heavily undersampling of the PIV does not allow to extract the underlying dynamics of the flow, the space-only HPOD is capable of delivering spatial modes, which are compatible with advecting features. This can be better appreciated if an oscillatory model of these modes is produced by multiplying these complex-valued spatial modes by the complex exponential $\exp(i\varphi)$, where φ is the temporal phase of the wave motion. Frames of the oscillatory model for the first, second, and third modes are provided in the first, second, and third columns of Fig. 18, respectively. The oscillatory model clearly shows the advecting behavior underlying the spatial modes delivered by the space-only HPOD, even if the actual behavior in time—likely characterized by modulation in frequency and amplitude—cannot be extracted.

IV. CONCLUSIONS

This paper explores a complex-valued extension of the POD dubbed Hilbert POD (HPOD), and in particular introduces a novel space-only variant capable of retrieving spatiotemporally coherent wave-packet structures also in the absence of temporally resolved data. Even in its conventional

version, this decomposition has found very little application in the field of fluid mechanics so far. The present work aims at stressing the potential that this technique has, in particular regarding its capability to identify wave-packet structures in flows that are dominated by advective instabilities.

The mathematical framework supporting the HPOD is extensively discussed, in particular introducing the concept of analytic signal computed through the Hilbert transform. The analytic signal is shown to be capable of retrieving the complex-valued mathematical representation of a traveling wave packet, expressed as a complex exponential, from its real-valued part, which is the only one available from either measurements or simulations. Using this concept, the Hilbert POD is introduced. This decomposition, as the name suggests, is based on the complexification of the dataset through the analytic signal concept, prior to performing a standard POD. The conventional HPOD performs the Hilbert transform in the temporal direction. In this paper, we explored the possibility to compute the HPOD from the Hilbert transform performed in the spatial advection direction. This variant has been referred to as *space-only*, since it only requires spatial resolution in the data, in contrast to conventional HPOD where temporal resolution is required. Using the mathematical framework introduced, it is demonstrated mathematically that the decomposition of the complexified dataset provides complex-valued temporal and spatial modes, which inherit the property of being analytic signals in the temporal or spatial direction, depending on which direction the Hilbert transform is performed in. These modes are therefore describing a complex exponential with local/instantaneous frequency and amplitude, thus representing the temporal or spatial function of a complex-valued wave packet. It is worth remarking that, differently from other complex-valued decompositions such as the spectral POD, the spectral content of the modes has a local/instantaneous character and is not spectrally pure: this property allows the HPOD to deal with modulation and intermittency phenomena in the data at the cost of a less trivial description of the dataset. Additionally, thanks to the similarity between advection time and space for a traveling wave packet, it is demonstrated that computing the analytic signal in the advective direction or in time allows to extract equivalent spatiotemporally coherent structures: when a link between the temporal frequency and spatial wave number exists in terms of a phase velocity, the conventional HPOD will provide analytic spatial modes and the space-only HPOD would provide analytic temporal modes. This concept ensures that the retrieved structures are spatiotemporally coherent, and it paves the way to identifying spatiotemporally coherent wave patterns also from non-time-resolved data using the space-only HPOD. Moreover, this concept can be used to discriminate between advective structures and other time-varying phenomena by using the most convenient direction to compute the analytic signal for the given flow scenario. Particularly, applying the space-only HPOD in the direction of propagation of a wave would allow to target said wave more specifically.

Both the conventional HPOD (in time) and the space-only HPOD (in the advective direction) are tested on three example problems in order to exemplify the properties of the decompositions and to test their performance.

The first example problem is the velocity field in the wake of a cylinder at a Reynolds number of 100 obtained through DNS. This dataset is characterized by a vortex shedding with a pure shedding frequency and a compact reduced order model, as well as by the availability of temporal resolution. For this dataset, it is shown that both implementations of the HPOD provide complex-valued modes, which represent the vortex shedding as wave packets with constant frequency in time. The results are compared to standard real-valued POD, showing that for this very simple dataset the real and imaginary part of the HPOD modes correspond to subsequent pairs of real-valued POD modes. Additionally, this dataset is exploited to exemplify two other concepts: (i) signal conditioning, typically in the form of signal ends trimming, is required to remove edge effects introduced by the Hilbert transform operation and avoid corruption of the HPOD; (ii) removing the temporal coherence from the dataset by shuffling the original time series does not allow the computation of conventional HPOD but does not alter the results of the space-only variant. This shows that both conventional and space-only HPOD—differently from space-only POD—can automatically deliver spatiotemporally coherent structures, without needing to pair together modes. The space-only HPOD variant, in particular, can be adopted also in datasets with reduced temporal resolution.

One obvious application of this space-only variant, therefore, is on a snapshot PIV dataset, which typically offers great spatial resolution but does not allow temporal information to be gathered. Note, however, that even though the conventional HPOD fails to recognize correctly the mode pairing, when applied in a low temporal resolution setting, it will safely revert to a solution equivalent to the standard POD one.

The second example problem is the time-resolved velocity field of a turbulent jet at a Reynolds number of 10^6 obtained through LES. Differently from the first example, this dataset is dominated by wave packets happening at multiple scales and characterized by a complex dynamics involving modulation phenomena and intermittency. Both variants of HPOD applied to this dataset retrieve practically identical complex-valued modes in time and space, which represent wave packets. The spatial modes are characterized by a wavelike pattern in the advective direction, and amplitude and frequency modulation in the same direction. The temporal patterns are similarly characterized by modulation of amplitude and frequency as well, and clearly show the presence of intermittency of the retrieved wave packets. Both spatial and temporal modes are analytic, i.e., are characterized by a spectral content limited only to the positive or negative side of the frequency spectrum. The sign of the spatial wave number and temporal frequency of the modes is compatible with a phase velocity of the wave packet directed in the advection direction. Despite the fact that the spatial and temporal modes are not spectrally pure, the space-wave number and time-frequency analysis reveal that the spectral content is narrow-banded, further reinforcing the idea that the HPOD targets advective structures. The capability of the HPOD to absorb modulation effects sets the present techniques apart from other techniques employed to identify advecting structures: differently from SPOD, where the temporal frequency of each spatiotemporal structure is fixed on an infinite temporal support, the HPOD provides spatiotemporal structures with instantaneous frequency. As such, the difference between the two decompositions is akin to the difference between Fourier analysis and time-frequency analysis, making them suited for different scopes. While the SPOD can offer a clear and simple overview of flow behavior in the space of frequencies, the HPOD trades this simpler description of the flow to offer the capability of capturing spatiotemporally coherent wave packets, whose frequency/wave number and amplitude are both local and instantaneous. This capability, for example, could be exploited to gather further insights into phenomena such as modulation and intermittency of turbulent flow features.

The third example problem is the velocity field of a turbulent jet at Reynolds number 33 000 measured by means of snapshot 2D PIV. This dataset represents a similar flow problem to that of the previous dataset, characterized by multiple scales and complex dynamics. The main difference is represented by the source of the dataset, which removes the availability of temporal resolution and introduces measurement uncertainty to the data. In this setting, the space-only HPOD is shown to retrieve spatial modes very similar to the ones identified in the LES dataset, confirming the capability of this variant to provide a physically meaningful decomposition even without accessing to temporal resolution. Indeed, the space-only HPOD can only provide a clear picture of the spatial modes, while the temporal ones do not allow to extract further information due to a lack of temporal resolution. This spatial information, however, can still be especially valuable when paired with techniques for extracting the flow dynamics. For simpler flows, characterized by a spectrally pure temporal frequency, oscillators models [16] can be built directly from the HPOD modes. For more complex flows, techniques developed for the space-only POD, such as Galerkin-POD projections models [60,61] or techniques based on the correlation with high-repetition-rate sensors (see POD-based stochastic estimators such as the Extended POD [62–65]), can be extended to the HPOD to provide more robust results in identifying a flow dynamic model.

ACKNOWLEDGMENTS

This work has been supported by the projects ARTURO, Grant No. PID2019-109717RB-I00, and EXCALIBUR, Grant No. PID2022-138314NB-I00, funded by MCIN/AEI/10.13039/501100011033 and by "ERDF A way of making Europe." M.R. is supported

by an Humboldt Research Fellowship for Experienced Researchers funded by the Alexander von Humboldt Foundation.

DATA AVAILABILITY

The data that support the findings of this article are openly available [66]. A MATLAB implementation of the HPOD is available at [67].

[1] C. W. Rowley and S. T. M. Dawson, Model reduction for flow analysis and control, Annu. Rev. Fluid Mech. **49**, 387 (2017).
[2] K. Taira, S. L. Brunton, S. T. M. Dawson, C. W. Rowley, T. Colonius, B. J. McKeon, O. T. Schmidt, S. Gordeyev, V. Theofilis, and L. S. Ukeiley, Modal analysis of fluid flows: An overview, AIAA J. **55**, 4013 (2017).
[3] A. E. Perry, M. S. Chong, and T. T. Lim, The vortex-shedding process behind two-dimensional bluff bodies, J. Fluid Mech. **116**, 77 (1982).
[4] P. Jordan and T. Colonius, Wave packets and turbulent jet noise, Annu. Rev. Fluid Mech. **45**, 173 (2013).
[5] R. E. A. Arndt, D. F. Long, and M. N. Glauser, The proper orthogonal decomposition of pressure fluctuations surrounding a turbulent jet, J. Fluid Mech. **340**, 1 (1997).
[6] A. V. G. Cavalieri, P. Jordan, and L. Lesshafft, Wave-packet models for jet dynamics and sound radiation, Appl. Mech. Rev. **71**, 020802 (2019).
[7] J. Jiménez, Coherent structures in wall-bounded turbulence, J. Fluid Mech. **842**, P1 (2018).
[8] J. L. Lumley, The structure of inhomogeneous turbulent flows, in *Atmospheric Turbulence and Radio Wave Propagation*, edited by A. M. Yaglom and V. I. Tatarsky (NAUKA, Moscow, 1967), pp. 166.
[9] J. L. Lumley, *Stochastic Tools in Turbulence* (Academic, Press, San Diego, CA, 1970).
[10] G. Berkooz, P. Holmes, and J. L. Lumley, The proper orthogonal decomposition in the analysis of turbulent flows, Annu. Rev. Fluid Mech. **25**, 539 (1993).
[11] L. Sirovich, Turbulence and the dynamics of coherent structures. I. Coherent structures, Q. Appl. Math. **45**, 561 (1987).
[12] N. Aubry, On the hidden beauty of the proper orthogonal decomposition, Theor. Comput. Fluid Dyn. **2**, 339 (1991).
[13] N. Aubry, R. Guyonnet, and R. Lima, Spatiotemporal analysis of complex signals: Theory and applications, J. Stat. Phys. **64**, 683 (1991).
[14] M. Ben Chiekh, M. Michard, N. Grosjean, and J. C. Bera, Reconstruction temporelle d'un champ aérodynamique instationnaire à partir de mesures PIV non résolues dans le temps, in *Proceedings of 9ème Congrès Francophone de Vélocimétrie Laser, Brussels, Belgium* (2004).
[15] M. Raiola, A. Ianiro, and S. Discetti, Wake of tandem cylinders near a wall, Exp. Therm. Fluid Sci. **78**, 354 (2016).
[16] A. G. Nair, S. L. Brunton, and K. Taira, Networked-oscillator-based modeling and control of unsteady wake flows, Phys. Rev. E **97**, 063107 (2018).
[17] P. J. Schmid, Dynamic mode decomposition of numerical and experimental data, J. Fluid Mech. **656**, 5 (2010).
[18] B. O. Koopman, Hamiltonian systems and transformation in Hilbert space, Proc. Natl. Acad. Sci. USA **17**, 315 (1931).
[19] M. Budišić, R. Mohr, and I. Mezić, Applied koopmanism, Chaos **22**, 047510 (2012).
[20] I. Mezić, Analysis of fluid flows via spectral properties of the Koopman operator, Annu. Rev. Fluid Mech. **45**, 357 (2013).
[21] J. H. Tu, Dynamic mode decomposition: Theory and applications, Ph.D. thesis, Princeton University, 2013.

[22] A. Towne, O. T. Schmidt, and T. Colonius, Spectral proper orthogonal decomposition and its relationship to dynamic mode decomposition and resolvent analysis, J. Fluid Mech. **847**, 821 (2018).
[23] M. Sieber, C. O. Paschereit, and K. Oberleithner, Spectral proper orthogonal decomposition, J. Fluid Mech. **792**, 798 (2016).
[24] M. A. Mendez, M. Balabane, and J.-M. Buchlin, Multi-scale proper orthogonal decomposition of complex fluid flows, J. Fluid Mech. **870**, 988 (2019).
[25] U. Grenander, *Toeplitz Forms and their Applications* (University of California Press, Berkeley, 1958).
[26] J. Kriegseis, M. Kinzel, and H. Nobach, Hilbert transform revisited–proper orthogonal decomposition applied to analytical signals of flow fields, in *Proceedings of the 14th International Symposium on Particle Image Velocimetry* (2021), Vol. 1, https://ispiv21.library.iit.edu/index.php/ISPIV/article/view/113.
[27] S. L. Hahn, *Hilbert Transforms in Signal Processing* (Artech House, 1996).
[28] K. R. Sreenivasan, On the fine-scale intermittency of turbulence, J. Fluid Mech. **151**, 81 (1985).
[29] R. Mathis, N. Hutchins, and I. Marusic, Large-scale amplitude modulation of the small-scale structures in turbulent boundary layers, J. Fluid Mech. **628**, 311 (2009).
[30] S. Karami, P. C. Stegeman, V. Theofilis, P. J. Schmid, and J. Soria, Linearised dynamics and non-modal instability analysis of an impinging under-expanded supersonic jet, J. Phys.: Conf. Ser. **1001**, 012019 (2018).
[31] Y. Huang, F. G. Schmitt, Z. Lu, and Y. Liu, An amplitude-frequency study of turbulent scaling intermittency using empirical mode decomposition and Hilbert spectral analysis, Europhys. Lett. **84**, 40010 (2008).
[32] Y. X. Huang, F. G. Schmitt, Z. M. Lu, P. Fougairolles, Y. Gagne, and Y. L. Liu, Second-order structure function in fully developed turbulence, Phys. Rev. E **82**, 026319 (2010).
[33] Y. X. Huang, F. G. Schmitt, J.-P. Hermand, Y. Gagne, Z. M. Lu, and Y. L. Liu, Arbitrary-order Hilbert spectral analysis for time series possessing scaling statistics: Comparison study with detrended fluctuation analysis and wavelet leaders, Phys. Rev. E **84**, 016208 (2011).
[34] Y. Huang, L. Biferale, E. Calzavarini, C. Sun, and F. Toschi, Lagrangian single-particle turbulent statistics through the Hilbert-Huang transform, Phys. Rev. E **87**, 041003(R) (2013).
[35] T. P. Barnett, Interaction of the monsoon and pacific trade wind system at interannual time scales Part I: The equatorial zone, Mon. Weather Rev. **111**, 756 (1983).
[36] T. P. Barnett, Interaction of the monsoon and pacific trade wind system at interannual time scales Part II: The tropical band, Mon. Weather Rev. **112**, 2380 (1984).
[37] T. P. Barnett, Interaction of the monsoon and pacific trade wind system at interannual time scales. Part III: A partial anatomy of the southern oscillation, Mon. Weather Rev. **112**, 2388 (1984).
[38] J. D. Horel, Complex principal component analysis: Theory and examples, J. Appl. Meteorol. Climatol. **23**, 1660 (1984).
[39] R. L. Pfeffer, J. Ahlquist, R. Kung, Y. Chang, and G. Li, A study of baroclinic wave behavior over bottom topography using complex principal component analysis of experimental data, J. Atmos. Sci. **47**, 67 (1990).
[40] M. A. Merrifield and R. T. Guza, Detecting propagating signals with complex empirical orthogonal functions: A cautionary note, J. Phys. Oceanogr. **20**, 1628 (1990).
[41] S. Alessio, A. Longhetto, and L. Meixia, The space and time features of global SST anomalies studied by complex principal component analysis, Adv. Atmos. Sci. **16**, 1 (1999).
[42] B. F. Feeny, A complex orthogonal decomposition for wave motion analysis, J. Sound Vib. **310**, 77 (2008).
[43] I. J. Yeaton, S. D. Ross, G. A. Baumgardner, and J. J. Socha, Undulation enables gliding in flying snakes, Nat. Phys. **16**, 974 (2020).
[44] P. Leroy-Calatayud, M. Pezzulla, A. Keiser, K. Mulleners, and P. M. Reis, Tapered foils favor traveling-wave kinematics to enhance the performance of flapping propulsion, Phys. Rev. Fluids **7**, 074403 (2022).
[45] J. Zhan, H. Shi, Y. Wang, and Y. Yao, Complex principal component analysis of antarctic ice sheet mass balance, Remote Sens. **13**, 480 (2021).

[46] T. Bolt, J. S. Nomi, D. Bzdok, J. A. Salas, C. Chang, B. T. Thomas Yeo, L. Q. Uddin, and S. D. Keilholz, A parsimonious description of global functional brain organization in three spatiotemporal patterns, Nat. Neurosci. **25**, 1093 (2022).

[47] S. L. Brunton and J. N. Kutz, *Data-driven Science and Engineering: Machine Learning, Dynamical Systems, and Control* (Cambridge University Press, Cambridge, 2022).

[48] S. Glavaski, J. E. Marsden, and R. M. Murray, Model reduction, centering, and the Karhunen-Loeve expansion, in *Proceedings of the 37th IEEE Conference on Decision and Control (Cat. No. 98CH36171)*, Vol. 2 (IEEE, New York, 1998), pp. 2071–2076.

[49] C. W. Rowley and J. E. Marsden, Reconstruction equations and the Karhunen–Loève expansion for systems with symmetry, Physica D **142**, 1 (2000).

[50] C. W. Rowley, I. G. Kevrekidis, J. E. Marsden, and K. Lust, Reduction and reconstruction for self-similar dynamical systems, Nonlinearity **16**, 1257 (2003).

[51] J. Reiss, P. Schulze, J. Sesterhenn, and V. Mehrmann, The shifted proper orthogonal decomposition: A mode decomposition for multiple transport phenomena, SIAM J. Sci. Comput. **40**, A1322 (2018).

[52] J. Sesterhenn and A. Shahirpour, A characteristic dynamic mode decomposition, Theor. Comput. Fluid Dyn. **33**, 281 (2019).

[53] H. M. Ek, V. Nair, C. M. Douglas, T. C. Lieuwen, and B. L. Emerson, Permuted proper orthogonal decomposition for analysis of advecting structures, J. Fluid Mech. **930**, A14 (2022).

[54] M. P. Encinar and J. Jiménez, Momentum transfer by linearised eddies in turbulent channel flows, J. Fluid Mech. **895**, A23 (2020).

[55] O. T. Schmidt and T. Colonius, Guide to spectral proper orthogonal decomposition, AIAA J. **58**, 1023 (2020).

[56] L. Marple, Computing the discrete-time "analytic" signal via FFT, IEEE Trans. Signal Process. **47**, 2600 (1999).

[57] C. Zhou, L. Yang, Y. Liu, and Z. Yang, A novel method for computing the Hilbert transform with Haar multiresolution approximation, J. Comput. Appl. Math. **223**, 585 (2009).

[58] A. Towne, S. T. M. Dawson, G. A. Brès, A. Lozano-Durán, T. Saxton-Fox, A. Parthasarathy, A. R. Jones, H. Biler, C.-A. Yeh, H. D. Patel, and K. Taira, A database for reduced-complexity modeling of fluid flows, AIAA J. **61**, 1 (2023).

[59] M. Raiola and D. Ragni, Dynamic behaviour of wave packets in turbulent jets, in *Proceedings of the 13th International Symposium on Particle Image Velocimetry* (Munich, Germany, 2019), https://athene-forschung.unibw.de/doc/129152/129152.pdf.

[60] C. W. Rowley, T. Colonius, and R. M. Murray, Model reduction for compressible flows using POD and Galerkin projection, Physica D **189**, 115 (2004).

[61] V. Jaunet, E. Collin, and J. Delville, POD-Galerkin advection model for convective flow: Application to a flapping rectangular supersonic jet, Exp. Fluids **57**, 84 (2016).

[62] J. Boree, Extended proper orthogonal decomposition: a tool to analyse correlated events in turbulent flows, Exp. Fluids **35**, 188 (2003).

[63] C. E. Tinney, L. S. Ukeiley, and M. N. Glauser, Low-dimensional characteristics of a transonic jet. Part 2. Estimate and far-field prediction, J. Fluid Mech. **615**, 53 (2008).

[64] Z. Hosseini, R. J. Martinuzzi, and B. R. Noack, Sensor-based estimation of the velocity in the wake of a low-aspect-ratio pyramid, Exp. Fluids **56**, 13 (2015).

[65] S. Discetti, M. Raiola, and A. Ianiro, Estimation of time-resolved turbulent fields through correlation of non-time-resolved field measurements and time-resolved point measurements, Exp. Therm Fluid Sci. **93**, 119 (2018).

[66] M. Raiola and J. Kriegseis, Dataset of: "Hilbert proper orthogonal decomposition: A tool for educing advective wave packets from flow field data", Zenodo (2026), doi: 10.5281/zenodo.18961134.

[67] M. Raiola and J. Kriegseis, Hilbert proper orthogonal decomposition, Mathworks File Exchange (2026), https://www.mathworks.com/matlabcentral/fileexchange/183376-hilbert-proper-orthogonal-decomposition.